

Kinematics and Slip Rates of Faults in the Indo-Asian Collision Zone

Richard Styron, GEM Foundation (richard.styron@globalquakemodel.org)

Abstract

Some faults are slow, while others are fast

1 Introduction

A modern assessment of regional fault geometries and slip rates must take into account not only the observations made for individual structures but also the role of each structure in a fault network and its contribution to regional strain and strain rate fields.

In this paper, a regionally-integrated active fault database for the Indo-Asian collision zone [Figure 1] is presented as HimaTibetMap v.2.0. This represents a major update to HimaTibetMap 1.0 (R. Styron et al., 2010; Taylor & Yin, 2009). The most substantial changes are the addition of slip rates for every structure, informed by a high-resolution block model, and a complete remapping of the original HimaTibetMap database at a much higher resolution. However, in many regions new faults have been added to the database, and a few structures are also omitted, typically because evidence for them was lacking or they were not able to be placed within the block framework (i.e., they were interpreted as minor splay faults).

The work is motivated by the need for accurate and internally-consistent fault geometries, kinematics and slip rates for a new probabilistic seismic hazard model for China being constructed by the Global Earthquake Model Foundation (GEM). Consequently, this paper will focus on the kinematics of sub-regions of the study area, particularly those that are [elucidated] by the block modeling; this is intended to provide documentation for the fault data that inform the seismic hazard model. Unfortunately, less attention will be paid to the tectonic implications of these new data and interpretations to questions of geodynamics and orogenic evolution, however inseparable these may be in reality. The data and code are publicly available and it is hoped that they will be of utility to interested scientists.

The implications of certain findings for seismic hazard will also not be discussed quantitatively or in much detail. These discussions will instead be found in a forthcoming publication describing the seismic hazard model, where they may be placed within a quantitative context.

1.1 Tectonic overview

The orogen is notable for the number of great (>1000 km) strike-slip faults that are located well away from the boundary between the Eurasian and Indian plates (located at the Main Himalayan Thrust and Sagaing fault). This list includes the Talas-Ferghana, Karakoram, Altyn Tagh, Jiali-Red

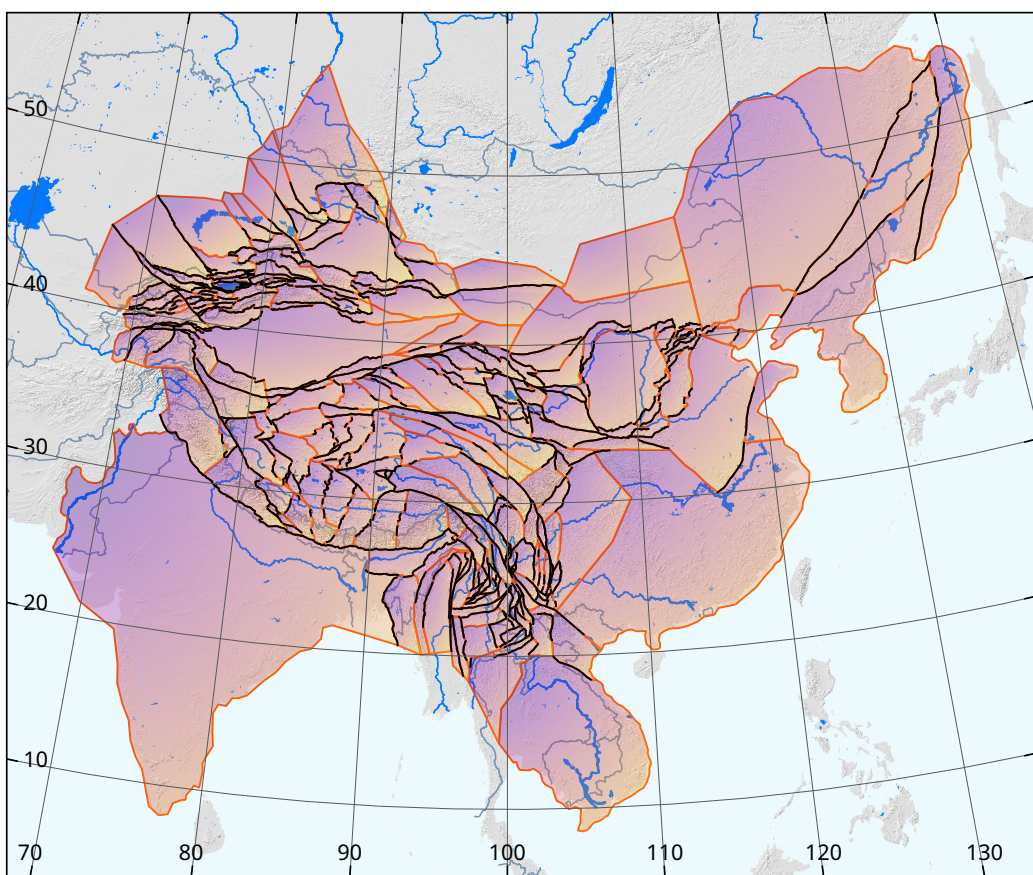


Figure 1: Faults and block model of the study area.

River, Xianshuehe-Xiaojiang, Kunlun and Haiyuan fault systems. The 3000+ km Yitong-Yulang fault system in northeastern China is perhaps outside of the orogen but longer still. No other contemporary orogen offers this breadth of strike-slip faulting.

2 Methods

The fault data and slip rates presented here were produced through a joint mapping–block modeling process. Faults and blocks were mapped in a Geographic Information Systems (GIS) program, and the block modeling was performed with the program Oiler, which was largely developed during this project.

2.1 Fault and block mapping

Faults and blocks were mapped in QGIS [qgis_ref], broadly simultaneously, on 30 m Shuttle Radar Topographic Mission topographic data and derivatives (primarily hillshades) and satellite imagery aggregated by Google, projected into QGIS using [wms/plugin/whatever]. Relevant publications, particularly field studies, and existing digital fault data (HimaTibetMap, GEM Global Active Faults Database) were frequently consulted as references but generally not viewed during mapping, to encourage a fresher evaluation of fault trace locations as expressed in the high-resolution topography. Nonetheless, the resulting mapping tends to be quite consistent between different mappers.

Because little has been written about the construction of fault and block models from a methodological standpoint, and surely variations exist among workflows, the process used here will be described in hopes that it may give some clarity to those who may undertake similar tasks.

The workflow used here is an iterative process. First, fault traces for some region were mapped in a draft GIS dataset, based on previous work and the topographic expressions of faulting. Indicators for faulting at any time in the past, as would be preserved in the bedrock by obvious juxtaposition of rock units, offset markers, preferential erosion along faults, were considered, primarily to gauge the location and kinematics of potentially active faults. Then, I looked for signs of Quaternary faulting such as the disruption of young sedimentary deposits and very sharp fault scarps. A more full treatment of the methods used to evaluate the activity of faults is given by R. Styron et al. (2020).

Next, blocks were created in a separate GIS layer of Polygon type. Blocks were drawn [].

Drawing blocks requires the explicit connection of disconnected faults. These connections may be obvious, but hard to localize directly (perhaps where faulting is distributed or hidden by rugged terrain or areas of rapid sedimentation). In other cases, the connections may be obscure and drawing them may seem capricious. The choice of if and where to connect faults is dependent on the clarity of connections in the terrain, as well as aspects of the available geologic and geodetic data. If geodetic stations are numerous and dense, and fault slip rates are known, then the motions of many small blocks may be well constrained. If faults are unclear in the landscape and unstudied, and geodetic stations are sparse, it may be beneficial to characterize an area with a few large blocks.

However, the size of blocks has a direct effect on the resulting slip rates. Given a fixed strain budget across a large region and sparse data inside the region, larger blocks will allocate the strain

at a smaller number of boundaries and therefore increase the mean slip rates at the boundaries, whereas smaller blocks will have slower slip rates on a large number of faults.

Longer connections are typically drawn to follow likely paths, rather than as straight lines in between faults. Shorter connections may be straight lines and often represent relays between en-echelon faults.

After blocks were drawn, faults were re-mapped

This process was performed iteratively and regionally. Typically, a small number of faults, usually fewer than ten, would be drafted. Then, block polygons were drawn connecting those faults,

This workflow offers benefits and [costs] compared to others. The methods here rely heavily on time-intensive geologic mapping and the subjective judgement of the mapper, but offer great detail

[Evans] have developed a method where disconnected faults are drawn, and block geometries are quantitatively evaluated by rigorous testing of the fits of geodetic data to [blarg]. The methods

2.2 Fault and geodetic data compilation

2.2.1 GNSS data compilation

GNSS data was compiled from several recent compilations and other studies. The main dataset used was assembled by M. Wang & Shen (2020) and is primarily a new solution for data from the extensive Crustal Movement Observation Network of China (CMONOC) as well as from other regional studies. Additional data outside of China were provided by the compilation by Kreemer et al. (2014) and Metzger et al. (2020). Data from sites

2.2.2 Geologic slip rates

Almost 200 Quaternary geologic slip rates were compiled for this study from the literature, in what is hoped to be a comprehensive collection. These use neotectonic techniques, where rates are estimated by measuring and dating offset geologic or geomorphic markers, rather than slip rates derived from paleoseismology, which may yield inaccurate slip rates if fewer than 5-10 events are measured R. Styron (2019). Rates were compiled if the study sites could be precisely located in topographic or satellite imagery, or if the study included spatial coordinates. As explained in Section 2.3, the point locations of slip rate sites are used in the block inversion, rather than slip rates ascribed more generally to some fault or fault section; this is important as slip rates may change along strike if an Oiler pole describing block motion is close to the block boundary. This requirement unfortunately prevents the use of a few slip rate studies, particularly older studies and those from the Chinese literature (which may have identifying information that I cannot translate).

Of the 188 compiled Quaternary slip rates, more than three quarters (158) were used in the inversion. Rates were not used if they were too far away from a fault in the study (such as on a minor splay), or [other geom problems]. In some other cases, rates were not used if the study uses dating assumptions that have been later shown to be problematic, yielding rates that are in conflict with other observations and inferences. Many of the studies of strike-slip faults before the late 2000s utilize flights of fluvial terraces that are differentially offset, and treat the (younger) lower terrace ages as the date of zero offset of the terrace riser rather than the (older) upper terrace age, which has the potential to greatly overestimate slip rates. Following Lensen

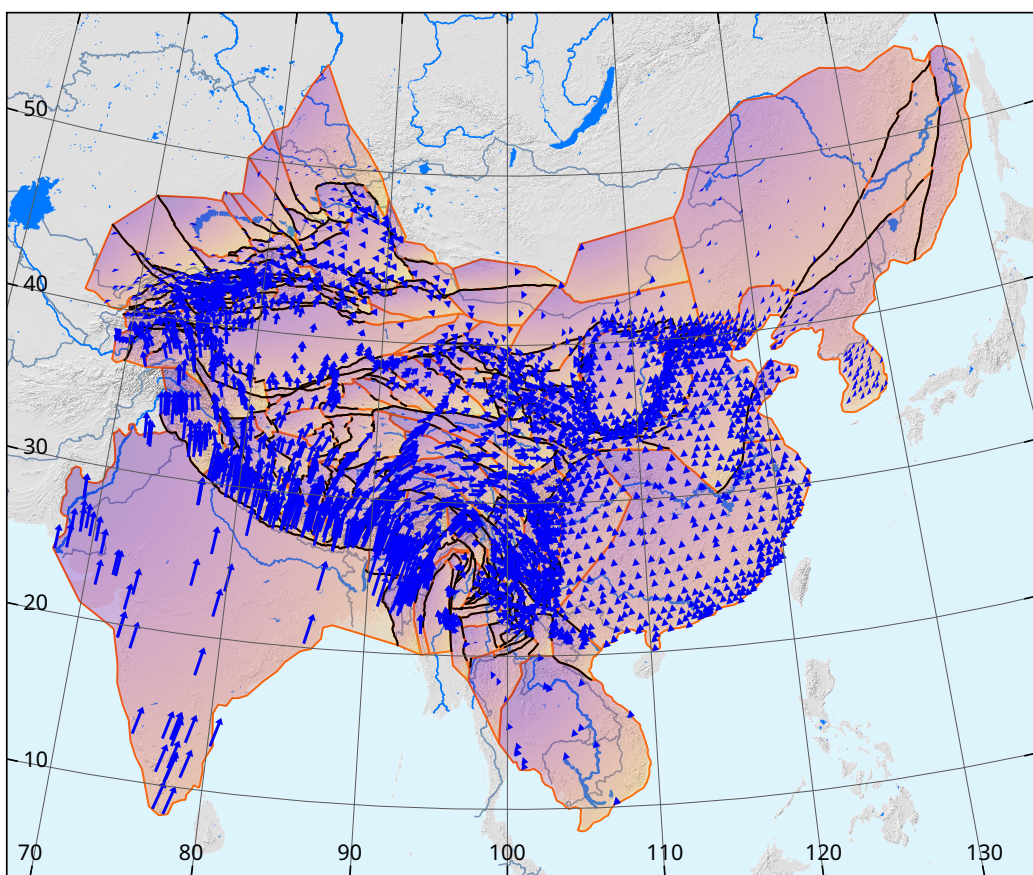


Figure 2: GNSS velocities used in the study.

(1964), Cowgill (2007) and Gold et al. (2009) systematically studied the reconstruction process and found that using the upper terrace ages for many Tibetan faults increases the congruence with slip rates from other datasets. Similarly, some older studies use charcoal from sag ponds or tectonically dammed drainages to estimate the age since the drainages were unmodified (e.g., Burtman et al., 1996) though subsequent investigation (e.g., Rizza et al., 2019) has shown that these dates more likely record the timing of the most recent surface-breaking earthquake, and that the measured offsets have been accumulating for much longer. This category of error also yields slip rates that are much higher than rates observed by other means. Other studies do not directly date the earth materials that are offset but infer ages based on climate events; these are not here considered reliable.

2.3 Block modeling

The block model computations were performed using *Oiler*, a block modeling package written in the Julia language, a relatively new programming language designed for high-performance numerical computing [[julia ref](#)]. *Oiler* is free and open-source software (see **Data and Resources** for more information).

Oiler solves for the best-fit poles of rotation (Euler poles) of the blocks via an inversion of GNSS velocities and Quaternary fault slip rates. *Oiler* draws heavily from previous work in this domain, particularly the mathematical formulations of Meade & Loveless (2009), Chase (1972), and Cox & Hart (1986). The work by Meade & Loveless (2009) was most influential. Meade & Loveless (2009) describe a linearization of the problem of solving for Euler poles given velocity observations on a spherical Earth, such that Euler poles are the solution to a system of linear equations based on the velocity observations. This linearization allows one to solve the system for the globally optimal Euler pole parameters using the extremely common and well-optimized linear regression techniques, obviating the need for more complex and computationally-intensive nonlinear optimization used by many previous workers [Chase (1972); [minster_jordan_mccaffrey](#)]. Fault slip rates in this framework are linear functions of the relative motions of the blocks on either side of a fault, so they are predicted by the Euler pole solutions. Additionally, several algorithms in *Oiler* were adapted from the *Blocks* code (written in MATLAB®) described by Meade & Loveless (2009). However, some fundamental differences exist between *Oiler* and *Blocks*: primarily, *Oiler* does not employ a reference frame or block for the block motions, such that the system solves for the rotations of each block with respect to this reference frame; instead, the relative block motions of pairs of blocks are solved for directly..

The solution strategy used by *Oiler* is to create a set of equations from each velocity observation that can be solved to find the parameters of the Euler pole describing the block rotations that the velocity is associated with. Both GNSS velocities and fault slip rates are considered velocities, and are treated similarly (though not identically) in the inversion. GNSS velocities result from the rotation of the blocks upon which the GNSS stations are located, with respect to some reference block that may or may not be spatially in the model, and are subject to the effects of the earthquake cycles of faults in the model (i.e., interseismic locking) [e.g., [savage](#); Meade & Loveless (2009)]. (Postseismic effects are not included in the model, and coseismic effects are in principle removed from the velocities by the data compilers.) Geologic slip rates, which are generally measured at a single point along a fault, are considered to be velocities resulting from the rotation of one fault block relative to the other fault block. If the geologic slip rate captures more than a few earthquake cycles, the rate can be considered to be free of earthquake-cycle variability (R. Styron, 2019).

2.3.1 Preparation of velocity observations

Oiler uses two types of velocity data in the inversion, GNSS velocities and fault slip rates. The GNSS data need little preparation; the east (V_E) and north (V_N) components of the velocities and their uncertainties are used directly, and the vertical component is considered to be zero.

Fault slip rates require some conversion to horizontal velocity vectors in order to be used. If both strike-slip and horizontal shortening or extension (i.e., heave) rates are given, a velocity vector in fault-normal and fault-parallel coordinates is rotated into east and north coordinates, such that the hanging wall is fixed and the footwall moves (vertical strike-slip faults are given a dip of 89° towards an arbitrary side to ensure that the hanging and footwalls are defined). However, typically Quaternary fault slip rate studies only resolve a single component of deformation; in this case, the other component is given a rate of $0 \pm 5 \text{ mm a}^{-1}$.

There is also the issue of converting dip-slip rates to heave rates. Meade & Loveless (2009) take a simple trigonometric approach, where the dip-slip rate is the heave rate divided by the cosine of the fault dip. However, this leads to very high rates for steeply-dipping faults; it also implies that the dip-slip rate of a fault separating two blocks is always higher than the far-field convergence or divergence rates of the two blocks, and that the far-field vertical velocity difference is non-zero, i.e. the whole of one block uplifts or subsides relative to the other (which may be accurate in some instances but inconsistent for two blocks separated by a fault system that changes dip direction along strike). Instead, *Oiler* considers the dip-slip rate to be equal to the heave rate, which is physically realistic if the footwall undergoes flexural folding at the fault trace; in this case there is no far-field relative uplift or subsidence of the blocks.

2.3.2 Solutions strategy

A velocity vector $\mathbf{V} = [V_E \ V_N \ V_U = 0s]^T$ is related to an Euler pole (a vector in Cartesian coordinates centered at the Earth's center) $\boldsymbol{\Omega} = [\omega_x \ \omega_y \ \omega_z]^T$ through the equation

$$\mathbf{V} = \boldsymbol{\Omega} \times RP \quad (1)$$

where RP is the Cartesian representation of the coordinates of point P (in latitude and longitude, on the surface of a spherical Earth) (e.g., Chase, 1972; Cox & Hart, 1986).

Meade & Loveless (2009) transform Equation 1 into a linear equation by using linear operators \mathbf{Pv} and \mathbf{Gb} that are functions of P in place of RP ; the product of these, \mathbf{G} , is a 3×3 matrix

$$\mathbf{G} = \mathbf{Pv} \cdot \mathbf{Gb} = \begin{bmatrix} G_{11} & G_{12} & G_{13} \\ G_{21} & G_{22} & G_{23} \\ G_{31} & G_{32} & G_{33} \end{bmatrix} \quad (2)$$

Then, Equation 1 can be represented as

$$\mathbf{G} \cdot \boldsymbol{\Omega} = \mathbf{V}. \quad (3)$$

When the velocity is known but the Euler pole is not, it may be derived by solving Equation 3 for $\boldsymbol{\Omega}$:

$$\hat{\boldsymbol{\Omega}} = \mathbf{G} \setminus \mathbf{V} \quad (4)$$

where the ‘backslash’ operator \setminus indicates an inverse solution, i.e. $\hat{\boldsymbol{\Omega}} = (\mathbf{G}^T \mathbf{G})^{-1} \mathbf{G}^T \mathbf{V}$, and the ‘hat’ symbol $\hat{\cdot}$ indicates an estimate.

The system to be solved involves N observations that constrain M poles. A larger system of equations can be constructed to solve for all of the poles simultaneously by grouping the matrices $G_1 \dots G_N$ and $V_1 \dots V_N$ by the pairs of blocks they are associated with. This is represented as the sparse matrix **BigG**, in which groups of \mathbf{G} matrices share the same columns, and each G occupies its own rows. The velocity observation matrices $V_1 \dots V_N$ are similarly stacked vertically as the column vector **BigV**, and the system is solved for the stacked pole vector **BigΩ̂**. When $M > N$ (as in this study), the system is overdetermined and the solution is the least-squares solution.

As an example, a system with six velocity observations $V_1 \dots V_N$ describing the relative motion of four plates A, B, C and D can be solved for the set of poles via the equation

$$\begin{bmatrix} {}^A\mathbf{G}_1^B & \mathbf{0} & \mathbf{0} & \mathbf{0} \\ {}^A\mathbf{G}_2^B & \mathbf{0} & \mathbf{0} & \mathbf{0} \\ \mathbf{0} & {}^B\mathbf{G}_3^C & \mathbf{0} & \mathbf{0} \\ \mathbf{0} & \mathbf{0} & {}^A\mathbf{G}_4^C & \mathbf{0} \\ \mathbf{0} & \mathbf{0} & {}^A\mathbf{G}_5^C & \mathbf{0} \\ \mathbf{0} & \mathbf{0} & \mathbf{0} & {}^B\mathbf{G}_6^D \end{bmatrix} \backslash \begin{bmatrix} {}^A\mathbf{V}_1^B \\ {}^A\mathbf{V}_2^B \\ {}^B\mathbf{V}_3^C \\ {}^A\mathbf{V}_4^C \\ {}^A\mathbf{V}_5^C \\ {}^B\mathbf{V}_6^D \end{bmatrix} = \begin{bmatrix} {}^A\hat{\boldsymbol{\Omega}}^B \\ {}^B\hat{\boldsymbol{\Omega}}^C \\ {}^A\hat{\boldsymbol{\Omega}}^C \\ {}^B\hat{\boldsymbol{\Omega}}^D \end{bmatrix}. \quad (5)$$

Note that the superscripts denote which blocks are involved, and the elements \mathbf{G} , \mathbf{V} and $\boldsymbol{\Omega}$ are matrices and vectors rather than scalars, and $\mathbf{0}$ is a 3×3 matrix of 0s, so **BigG** has 18 rows and 12 columns.

2.3.3 The effects of fault locking on geodetic velocities

GNSS geodetic velocities are the sum of both the long-term block motion (Equation 1) and the effects of interseismic fault locking on other faults in the model. As the standard approach, the effects of fault locking are modeled as an elastic dislocation on each fault equal to, but in the opposite sense of, the long-term fault slip rate.

As the slip rates of the faults are unknowns in the model, they are included in the inversion following methods adapted from Meade & Loveless (2009). The displacements at each GNSS site given unit slip on each linear segment of each fault, and the displacements from all of the faults associated with each Euler pole are summed and then added to **BigG** in the appropriate location.

As an example, if V_1 above is a GNSS velocity, and there are two faults in between Blocks A and B as well as three faults between Blocks B and C, then

$${}^A\mathbf{V}_1^B = {}^A\mathbf{G}_1^B + \sum_i^{n=2} ({}^A\mathbf{F}_i^B(P_1)) + \sum_i^{n=3} ({}^B\mathbf{F}_i^C(P_1)). \quad (6)$$

where ${}^A\mathbf{F}_i^B(P_1)$ is the displacement matrix at point P_1 resulting from unit slip on fault F_i (\mathbf{F} is a 3×3 diagonal matrix). The first sum would be added to the ${}^A\mathbf{G}_1^B$ term in **BigG**, and the second sum would be added to the $\mathbf{0}$ term immediately to the right.

These effects are only applied to GNSS velocities in the model; velocities from fault slip rates are unaffected.

Additionally, only mapped fault segments are used to calculate these effects; block boundaries that do not correspond to mapped faults are considered to be creeping. This contrasts with the approach of Meade & Loveless (2009) but is common in other block modeling systems [MCCAFFREY, ELLIOTT]. This choice allows non-fault block boundaries (which tend to be

inferred rather than known, in geologic mapping parlance) to be drawn more crudely, as the geometry of the boundary does not impact the inversion other than to specify which blocks each GNSS station is associated with. There are very few GNSS stations near long non-fault block boundaries in the model, so it is not expected that un-modeled earthquake cycle effects from these boundaries are biasing the model results.

2.3.4 Block velocity closure constraints

[The system] needs additional constraints to satisfy the block velocity closure constraints ${}^A\Omega^B + {}^B\Omega^C - {}^A\Omega^C = 0$ (Chase, 1972; Cox & Hart, 1986). An equality constraint matrix **CM** is constructed from equations describing this relationship for each component of Ω , e.g. ${}^A\omega_x^B + {}^B\omega_x^C - {}^A\omega_x^C = 0$. From the example above, the matrix would be

$$\mathbf{CM} = \begin{bmatrix} 1 & 0 & 0 & 1 & 0 & 0 & -1 & 0 & 0 & 0 & 0 & 0 \\ 0 & 1 & 0 & 0 & 1 & 0 & 0 & -1 & 0 & 0 & 0 & 0 \\ 0 & 0 & 1 & 0 & 0 & 1 & 0 & 0 & -1 & 0 & 0 & 0 \end{bmatrix}. \quad (7)$$

${}^B\Omega^D$ is not included in the block velocity circuit, so the right-most three columns, corresponding to ${}^B\Omega^D$, only contain zeros. **CM** is the left-hand side of the equality constraint, and is matched on the right-hand side by $\mathbf{0}^{CM}$, which is a column vector of zeroes with the same number of rows as **CM** ($\mathbf{0}^{CM}$ is a vector of Lagrange multipliers).

In the real model, all block velocity circuits are identified through a breadth-first search of a graph describing which blocks are linked through poles that correspond to a velocity observation. Any three blocks mutually separated by faults form a circuit, as do two blocks separated by a fault that each host GNSS stations in the same reference frame (a non-spatial block in the model). The matrix **CM** has stacked submatrices representing each circuit.

The final component to the inversion is the weight matrix **W**, which weights each observation proportionally to the inverse of the variance associated with each velocity observations.

The matrices **BigG**, **CM** and **W** are concatenated to form a larger system corresponding to an equality constrained, weighted least squares solution (Abdel-Aziz, 2006; Gulliksson & Wedin, 1992):

$$\begin{bmatrix} \mathbf{BigG} & \mathbf{0} & \mathbf{W} \\ \mathbf{CM} & \mathbf{0} & \mathbf{0} \\ \mathbf{0} & \mathbf{CM}^T & \mathbf{BigG}^T \end{bmatrix} \backslash \begin{bmatrix} \mathbf{BigV} \\ \mathbf{0}^{CM} \\ \mathbf{0} \end{bmatrix} = \begin{bmatrix} \mathbf{Big}\hat{\Omega} \\ b_1 \\ b_2 \end{bmatrix}. \quad (8)$$

The system is solved using an LU factorization of the design matrix with algorithms from *UMFPACK* (Davis, 2004). b_1 and b_2 are discarded.

2.3.5 Propagation of uncertainty

Uncertainties in the velocity observations are propagated to the Euler pole solution **Big** $\hat{\Omega}$ through Monte Carlo techniques.

Once the design matrix in Equation 8 is factorized, 1000 samples of **BigV** are drawn from the mean and standard deviation of each component of each velocity observation, and the system is solved iteratively. The covariance matrix $\Sigma_{Big\Omega}$ of **Big** $\hat{\Omega}$ is then constructed from the 1000 iterations of **Big** $\hat{\Omega}$ and the variance of the solution is

$$\sigma^2(\mathbf{Big}\hat{\Omega}) = \frac{\mathbf{e} \cdot \mathbf{e}'}{3N - 3M} \cdot \Sigma_{Big\Omega}. \quad (9)$$

where \mathbf{e} is the vector of residuals, and N and M are the numbers of velocity observations and poles, respectively (as above). The covariance matrix for each Euler pole Σ_Ω is extracted from the appropriate elements of $\sigma^2(\mathbf{Big}\hat{\Omega})$.

The uncertainties in the Euler poles are then propagated to the predicted velocities, and then finally to the faults. The covariance matrix for any velocity vector \mathbf{V} is calculated as $\Sigma_V = \mathbf{G} \cdot \Sigma_\Omega \cdot \mathbf{G}'$.

It should be noted that the uncertainties calculated here are only those resulting from the formal uncertainties on the velocity observations. The uncertainties that are related to uncertainties in the model construction (i.e., the location of faults or how the faults are connected to form blocks) are likely much larger, but are not quantified in this study. It is possible that they may be estimated through the exploration of weighted branches in a logic tree with nodes corresponding to

3 Results

3.1 Evaluation of model fits

Residuals are shown on regional maps, which help evaluate the quality of fit of the block model
...

4 Regional kinematics

4.1 Tien Shan

The Tien Shan is the northwesternmost deforming zone in the Indo-Asian collision zone. The mountain system undergoes N-S contraction through slip on E-striking reverse faults distributed throughout (e.g., Thompson et al., 2002), leading to a contractional basin and range physiography. The region is bound to the southwest by the Pamir, farther east by the rigid Tarim Basin, and in the north by the Kazakh shield, which is geodetically part of stable Eurasia. GNSS velocities in the northern margin of the Pamir and western Tarim Basin have northward components of ~ 20 mm a^{-1} , which decreases to about half of that in the eastern Tarim basin [Figure 4]; this is the shortening budget of the Tien Shan.

The distributed nature of deformation is evident in the contraction rates for individual structures (which range from $\sim 0.3\text{--}4$ mm a^{-1} [Figure 4], [refs]), and is well constrained by the dense coverage of both GNSS data and neotectonic slip rate measurements. As the contraction rates across the Tien Shan decrease by half to the east, the number of structures accommodating the shortening decreases, while the typical shortening rate on a given structure does not.

The highest shortening rates are found along the southern frontal thrusts, where the Tien Shan overrides the Tarim Basin; rates are consistently **2.5–4.0** mm a^{-1} along the western and central parts of the rangefront.

The modeling in this study also indicates that the Tien Shan extends east-west, as evident in the increasing eastward velocity of GNSS data. However, few structures are found that clearly accommodate this extension.

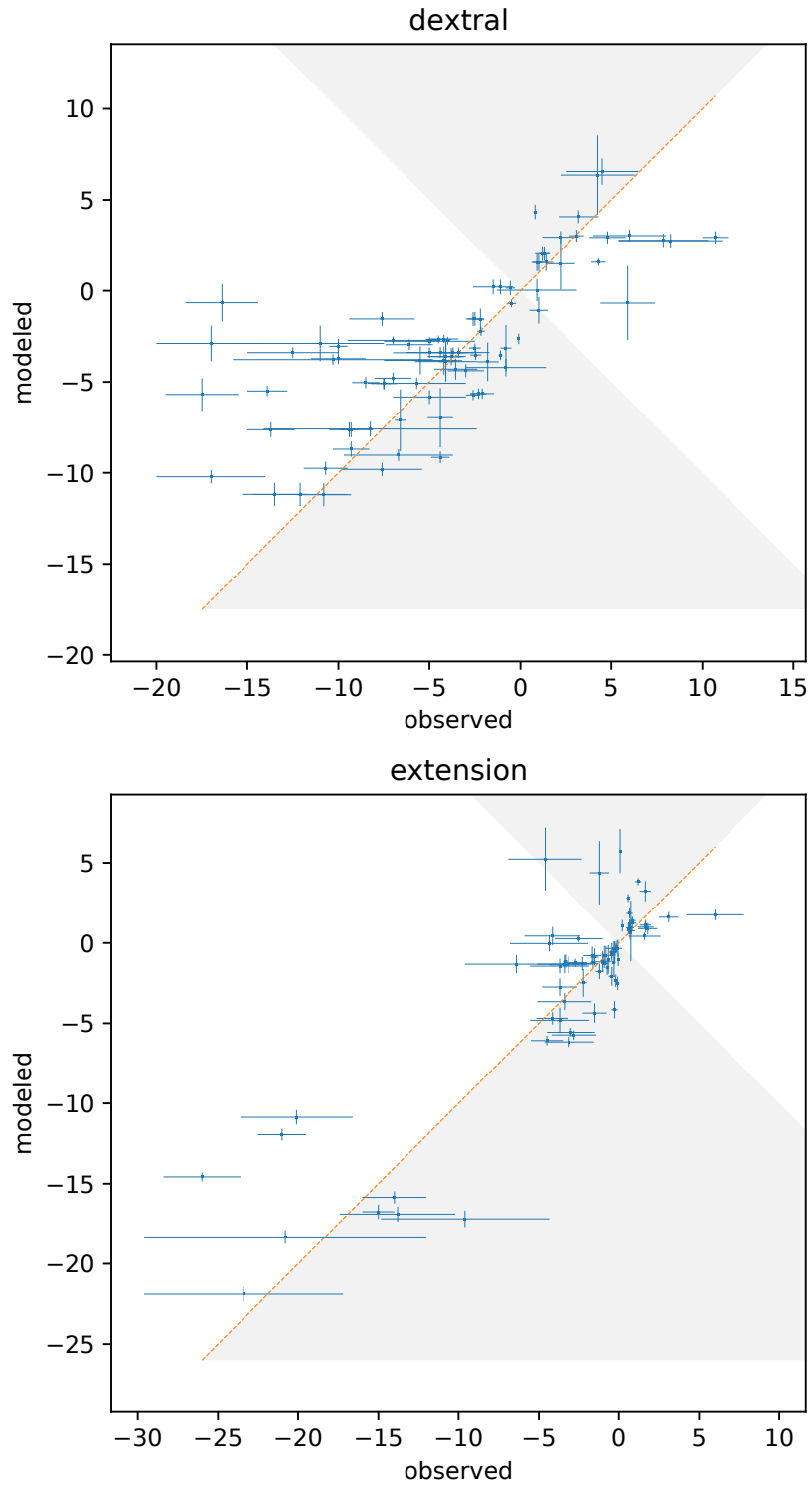


Figure 3: Comparison of modeled and observed geologic slip rates

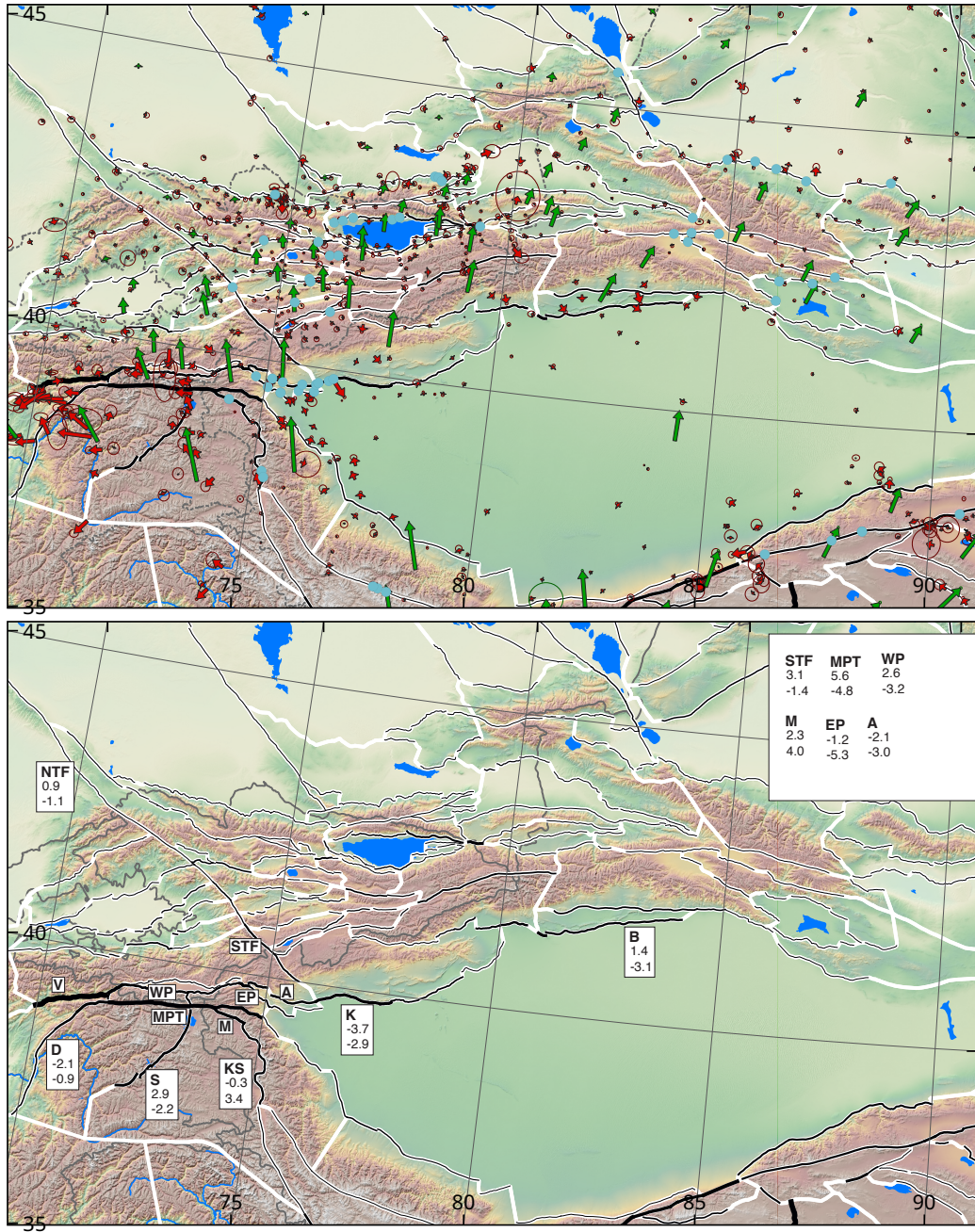


Figure 4: Tien Shan and Pamir. KZ = Kyrgyzstan. TF = Talas-Ferghana fault. VF = Vakhsh fault. MPT = Main Pamir Thrust. KKF = Karakoram fault. SF = Sarez fault.

4.1.1 NW-striking dextral faults

Several major NW-striking dextral faults cut through the Kazakh shield into the northern Tien Shan. The westernmost is the 1000 km long Talas-Ferghana fault, which bisects the range. The kinematic role and slip rate on the Talas-Ferghana fault has been contested through the decades. The earliest modern neotectonic slip rate estimates for the fault are $\sim 1 \text{ cm a}^{-1}$ (Burtman et al., 1996), in line with a few more modern estimates (e.g., Rust et al., 2018). However, geodetic studies (Metzger et al., 2020; e.g., Mohadjer et al., 2010; Zubovich et al., 2010) limit the slip rates to a few mm a^{-1} , as do other geologic studies. Rizza et al. (2019), for example, find low rates and demonstrate that the radiocarbon dates used to infer the age of undeformed stream channels on the fault may simply record the date of the last major earthquake.

I find rates consistent with the lower set of estimates; dextral rates are less than 0 mm a^{-1} at the northwestern end of the fault (also known as the Karatau fault (M. B. Allen et al., 2001)) and increase southeastward to about 3 mm a^{-1} . Dextral rate estimates of $\sim 1 \text{ cm a}^{-1}$ are inconsistent with the regional fault kinematics, as they would require most of the shortening in the Tien Shan to the east of the fault to be accommodated along the southern thrusts bordering the Tarim Basin, while to the west of the fault, the shortening would have to be accommodated north of the Ferghana basin in the Chaktal ranges; this is not supported by either the neotectonic slip rates or geodetic data within the Tien Shan demonstrating distributed shortening. Extension and contraction across the fault is variable, relating to stepovers and rotations of local blocks, but less than 2 mm a^{-1} .

Parallel strike-slip faults to the east terminate in the northern margins of the Tien Shan rather than in the interior of the ranges (e.g., Tapponnier & Molnar, 1979). Slip rates on the Dhzalair-Naiman, Aktas, and Lepsy faults all have rates in this solution well under 1 mm a^{-1} , though they have a clear topographic expression and yield evidence for large-magnitude if infrequent Holocene seismicity (e.g., Campbell et al., 2015).

Farther to the east, the Dzhungarian fault cuts through northern Tien Shan, bifurcating the Ala-Tau and Kertau ranges at the Dzhungarian Gate, before merging with thrusts south of the Dzhungarian basin. I find that the dextral slip rate increases from north to south, with a rate of $1.5 \pm 1.4 \text{ mm a}^{-1}$ in the Dzhungarian Gate, in agreement with the rate of $2.2 \pm 0.8 \text{ mm a}^{-1}$ found by Campbell et al. (2013).

The Ferghana Valley is an intermontane basin in the western Tien Shan, north of the Pamir and west of the Talas-Ferghana fault. The valley holds 12-15 million people (Borthakur, 2017), and is bound on the northern and southern margins by active thrusts; as such, it is the most populated region fully encapsulated by the orogen and a major source of seismic risk. The results of this study yield slip rates of $\sim 0.5\text{-}3 \text{ mm a}^{-1}$ on the thrusts surrounding the basin.

4.2 Pamir

The Pamir converges with the Alai ranges of the southeastern Tian Shan at the Alai Valley, the western margin of the Tarim basin to the east, and the northeastern margin of the Tajik basin to the west [Figure 4]. Shortening in this convergence zone is very rapid, with $8.2 \pm 1.5 \text{ mm a}^{-1}$ on the Main Pamir Thrust, $0.6 \pm 1.6 \text{ mm a}^{-1}$ on the Pamir Frontal Thrust, and $0.2 \pm 0.7 \text{ mm a}^{-1}$ on the Vakhsh fault bordering the northern Alai valley.

Extension is also relatively rapid, but decreases to the south. The Kongur Shan normal fault extends at $5.4 \pm 0.6 \text{ mm a}^{-1}$ (a bit higher than the geologic rates of $1.65 \pm 0.35 \text{ extension by}$

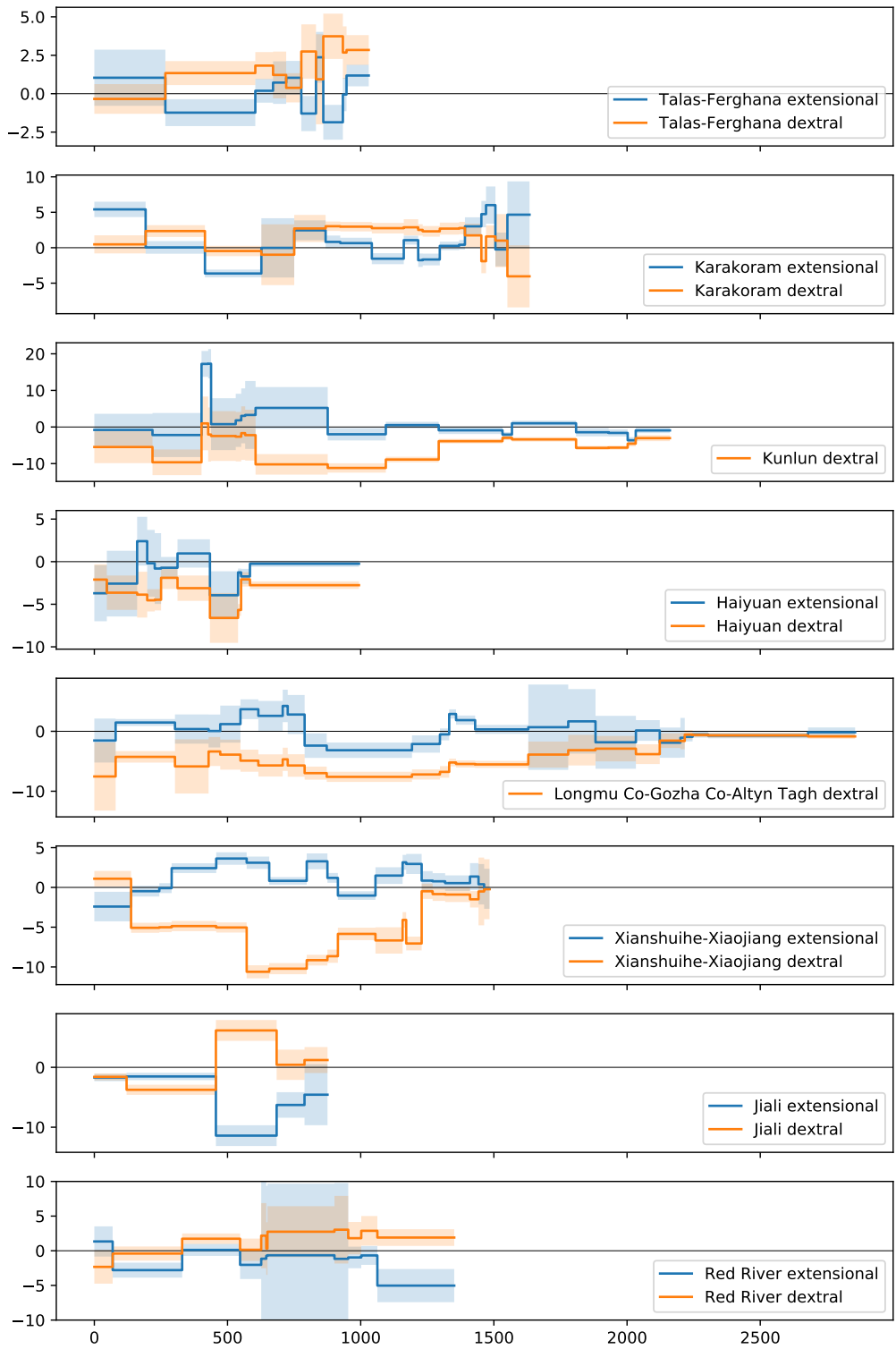


Figure 5: Slip rates for major strike-slip fault systems along strike. Dextral rates are in orange (negative rates are sinistral) and extensional rates are in blue (negative rates are contraction). 2- σ uncertainties are shown as pale envelopes around rates.

M.-L. Chevalier et al. (2015)), and the kinematically-linked Muji fault extends at 6.3 ± 1.0 mm a $^{-1}$, with dextral slip of 6.6 ± 0.7 mm a $^{-1}$, somewhat lower than the dextral rate from M.-L. Chevalier et al. (2011). The NE-striking Sarez fault cuts through the center of the Pamir, separating the eastern and western blocks at 5.3 ± 0.6 mm a $^{-1}$ sinistral slip in the south, which changes to about half that sinistral slip rate and an extension rate of 2.4 ± 1.0 mm a $^{-1}$ in the north where it meets the Main Pamir Thrust.

The northeast corner of the Tajik basin is bound in the east by the Darvaz fault, where it underthrusts the Pamir, and in the north by the Vakhsh fault, where it underthrusts the Alai ranges (e.g., Metzger et al., 2020). Slip rates near the Alai valley are high, with 8.0 ± 1.2 mm sinistral-reverse faulting on the Vakhsh fault matched by 10.6 ± 1.6 mm a $^{-1}$ dextral-reverse slip along the Darvaz fault. This is broadly consistent with the tectonic escape model proposed by Metzger et al. (2020) though our block modeling indicates that the Euler pole between the Tajik basin and the Pamir is relatively close by to the southeast, so that relative deformation rates decrease to the southwest.

4.2.1 Western Tarim Basin

The western Tarim Basin is bound by the Tien Shan to the north and the Pamir to the south. The thrusting in the Tarim foreland is somewhat complex, and the mapping here is more of a simplification than in other locations. Nonetheless, the major structures are resolved. The fastest-slipping structure in the region is the Atushi-Talanghe-Mutule anticline (here considered a north-dipping thrust merging into the Tien Shan) which has a shortening rate of 4.7 ± 0.7 mm/y in the west (quite consistent with the geologic rates by Scharer et al. (2004) and Thompson Jobe et al. (2017)) and decreases east to about half over 400 km. Additional thrusts in the complex convergence zone where the Pamir meets the Tien Shan are poorly constrained, but in general have somewhat slower slip rates than the geologic data.

4.3 Himalaya

Much of the convergence between India and Eurasia is accommodated on the Main Himalayan Thrust, which is the plate boundary fault separating the two continents [e.g., refs]. Though the Himalayan wedge is constructed of many stacked nappes separated by thrusts that have been active at various times throughout the Cenozoic [e.g., refs], most or all of the slip on the Main Himalayan Thrust is transferred to the Main Frontal Thrust at the very tip of the wedge and perhaps the Main Boundary Thrust that daylights a few tens of km towards the hinterland [mas refs]; these are uniformly interpreted to merge at depth. A longstanding body of research holds that additional out of sequence thrusts may be active in the interior of the Himalayan wedge, most prominently the Main Central Thrust in Nepal that separates the High Himalaya from the Lesser Himalaya [e.g., Hodges].

This study considers the Main Frontal Thrust and Main Himalayan Thrust to be one and the same, dipping at 10° , and does not include the Main Boundary Thrust, Main Central thrust, or other splays, with the exception of the Western Nepal Fault System described below. This simplification is due to the complexity of geodetic block modeling of vertically stacked splay faults that merge at depth. It is hoped that future work more focused on the Himalaya, rather than the entire orogen, may incorporate more structural complexity.

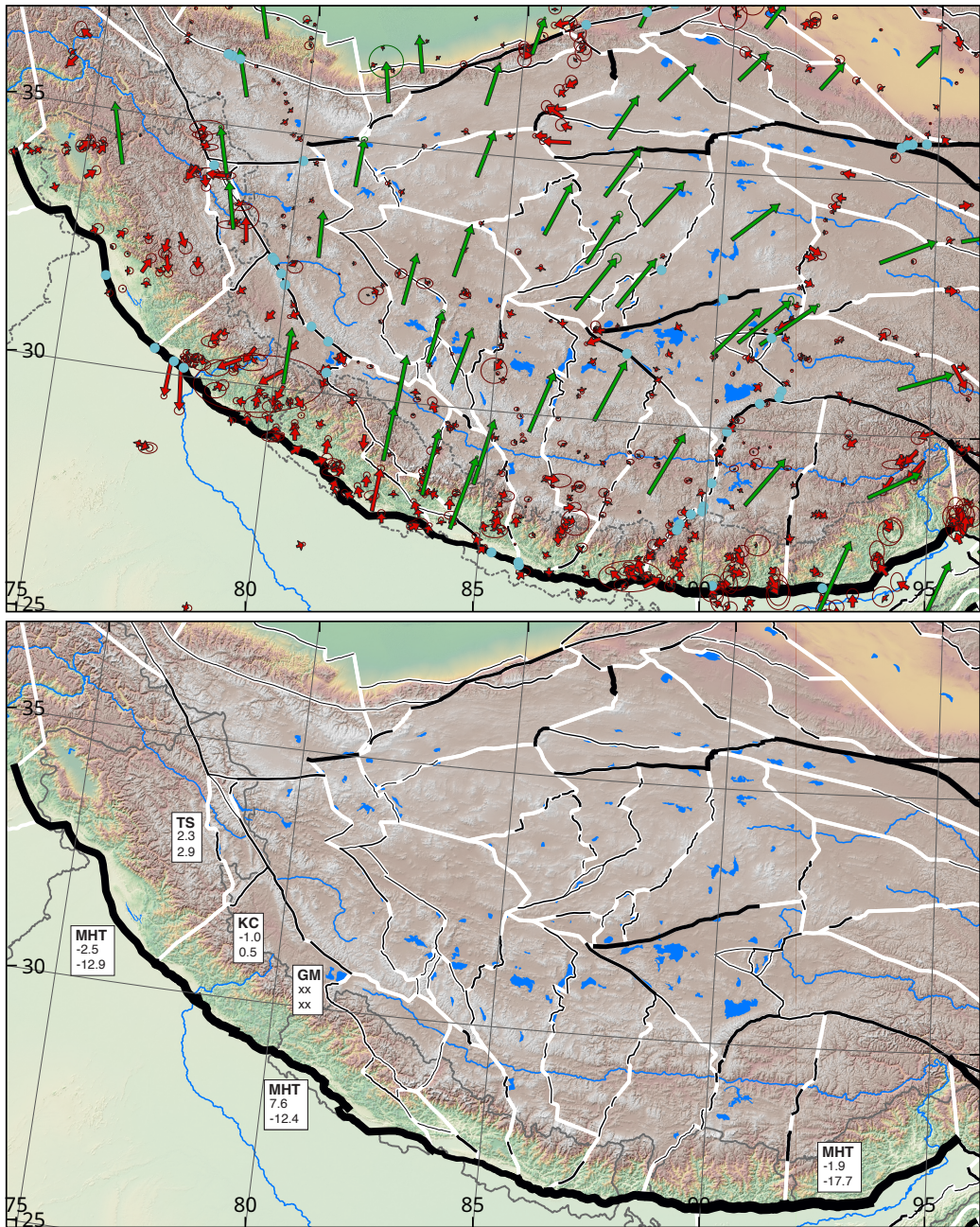


Figure 6: Himalaya and Tibet. MHT = Main Himalayan Thrust. WNFS = Western Nepal Fault System. TM = Tso Morari fault. KC = Kaurik-Chango fault. GM = Gurla Mandhata fault. TG = Thakkhola Graben. Y = Yadong rift. KF = Karakoram fault. L = Lunggar rift. LP = Lopukangri rift. YR = Yari rift. XG = Xiagangjiang rift. TYC = Tangra Yum Co rift. GZ = Garze fault. GC = Gyaring Co fault. PX = Pum Qu-Xainza rift. DX = Damxung graben. NQTL = Nyainqntanghla fault. CO = Cona-Oiga rift. EHS = Eastern Himalaya Syntaxis. BC = Beng Co fault. DNC = Dong Co fault. G = Gulu rift. DR = Daru Co fault. J = Jiali fault LC = Longmu Co fault. GZ = Gozha Co fault. YT = Yutian rift. SH = Shuang Hu graben. QX = Qixiang Co fault. ATF = Altyn Tagh fault.

4.3.1 Main Frontal Thrust

Estimates of slip rates on the Main Himalayan Thrust range between $\sim 10\text{-}20 \text{ mm a}^{-1}$ [e.g., refs], or about a third to a half of the total Indo-Asian convergence. Many authors consider that rates change along strike, increasing from the northwest, with geologic rates as $9 +7/ -3.5 \text{ mm a}^{-1}$ (Kumar et al., 2001), to over 20 mm a^{-1} in the eastern Himalaya (Burgess et al., 2012). These results broadly replicate that trend. The results for the northwest Himalaya (immediately south of the Thakkhola graben in central-western Nepal all the way to Pakistan) yield shortening rates between $14\text{--}17 \text{ mm a}^{-1}$, all within uncertainty of geologic rates (Kumar et al., 2001; Powers et al., 1998; Wesnousky et al., 1999). In the central Himalaya, between the Thakkhola graben and the Yadong rift, the shortening rates resolved here are slightly lower, $12\text{--}15 \text{ mm a}^{-1}$, which is a much poorer fit with geologic rates of $20\text{--}26 \text{ mm a}^{-1}$ (Bollinger et al., 2014; Lavé & Avouac, 2000), as well as with many geodetic rates, also around 20 mm a^{-1} (Ader et al., 2012; Stevens & Avouac, 2015). This discrepancy diminishes to the east, where I find contraction rates of $16\text{--}22 \text{ mm a}^{-1}$, in agreement with the geologic rates by Burgess et al. (2012) and Berthet et al. (2014).

Strike-slip deformation on the Main Himalayan Thrust is generally dextral in the northwest and central Himalaya, replicating observations from geology (Javed N. Malik et al., 2015; J. N. Malik & Nakata, 2003; Shah et al., 2021) and geodesy (Jouanne et al., 2004; Kundu et al., 2014; Stevens & Avouac, 2015), and sinistral in the east, but rates vary greatly segment to segment. The primary reason for the short-wavelength variability is moderate variations in the strike of adjacent segments, but some of it is likely due to larger-scale kinematics. In either case, it is unclear exactly how and where strike-slip deformation is accommodated. Focal mechanisms and coseismic finite fault models in the Himalaya are well partitioned into relatively pure dip slip on the thrusts and strike slip on structures in the hanging wall (e.g., Bendick et al., 2007; R. H. Styron et al., 2011), consistent with plate convergence zones globally (e.g., Jarrard, 1986; McCaffrey, 1994). However, the broader scale oblique partitioning models consider the Karakoram fault to be the locus of strike-slip deformation and backstop of a translating forearc sliver (McCaffrey & Nabelek, 1998; R. H. Styron et al., 2011); this analysis shows that the dextral slip rates on the Main Himalayan Thrust are as great or greater than on the Karakoram fault.

The discrepancy between coseismic evidence for slip partitioning and interseismic model indicating oblique strain accumulation is difficult to resolve. Geologic observations of dextral slip on splay faults within the frontal Himalayan wedge exist (Javed N. Malik et al., 2015; J. N. Malik & Nakata, 2003; Nakata, 1989; Shah et al., 2021; Silver et al., 2015) but most of these faults are within a few tens of kilometers of the frontal thrusts, and likely merge with the Main Himalayan Thrust at fairly shallow depths, well within its interseismically locked and putatively seismogenic boundaries; given a dip of around 10° , substantially oblique slip during a major earthquake on the Main Himalayan Thrust would be very surprising.

4.3.2 Intra-Himalayan faults

Several fault systems cut into or through the Himalaya. These are typically normal or oblique-normal fault systems that are linked with rifts in southern Tibet (e.g., Armijo et al., 1986; R. H. Styron et al., 2011), and divide the Himalaya into blocks that move with different velocity vectors relative to southern Tibet (McCaffrey & Nabelek, 1998; R. H. Styron et al., 2011).

In the west, the Tso Morari rift has about 2 mm a^{-1} of dextral-normal slip, while the neighboring Kaurik-Chango fault bounding the western Leo Parghil dome has 2 mm a^{-1} of normal slip.

The next major intra-Himalayan fault system to the southeast is the Gurla Mandhata rift, which

extends at $1.1 \pm 0.3 \text{ mm a}^{-1}$. The Western Nepal Fault System (Murphy et al., 2014) is thought to represent the propagation of slip on the Karakoram Fault southeastward through the Gurla Mandhata detachment to a set of ESE-striking faults that approach or merge with the Main Boundary Thrust (a splay fault of the Main Himalayan Thrust north of the Main Frontal Thrust). I find consistent dextral slip, with minor extension or contraction as fault orientation changes; a rate of 2.7 ± 0.4 from the center of the fault is typical.

The central and eastern Himalaya has several N-trending rifts. The most well-known of these are the Thakkhola graben in western Nepal and the Yadong rift on the Tibet-Bhutan border. The Thakkhola graben resolves here as sinistral ($-1.8 \pm 0.7 \text{ mm a}^{-1}$), with essentially zero extension ($-0.0 \pm 0.5 \text{ mm a}^{-1}$).

Extension along the Yadong rift ranges from $1.2 \pm 0.3 \text{ mm a}^{-1}$ in the Himalaya zone on the Bhutan border to $2.7 \pm 0.3 \text{ mm a}^{-1}$ farther north. These values are compatible with many of the geologic data which yield rates of about $0.5\text{--}2 \text{ mm a}^{-1}$ (inclusive of uncertainty) (Ha et al., 2019; S. Wang et al., 2020), and reflect a general pattern of northward-increasing extension on south Tibetan rifts.

A few other faults are mapped here in the central Himalaya, where the boundaries between south Tibetan blocks extend south to meet the Main Frontal Thrust. Faults have been drawn where the topography is suggestive, though to my knowledge these are not described in the literature; these are considered highly suggestive. These slip at a few mm a^{-1} , with variable kinematics.

The broader pattern of Himalayan block motions, manifest but perhaps not obvious in the fault slip rates, is that the range is undergoing ‘oroclinal unbending,’ where the broad curvature of the range in map pattern is decreasing. Essentially, the center of the range (central Nepal through Bhutan) is moving faster to the northeast than the eastern and northwestern flanks of the range. This results in sinistral slip along the NNE-striking intra-Himalayan rifts of western Nepal and India (the Thakkhola, Gurla Mandhata and Leo Parghil rifts).

4.4 Central Tibet

Faulting in central Tibet is dominated by east-west extension on ~N-striking normal faults, dextral-oblique slip on NW-striking faults, and sinistral-oblique slip on NE-striking faults (e.g., Taylor et al., 2003). Geodetic and geologic data is sparse in the region, particularly in the north. As a consequence, block motions here are not always well constrained, and in some cases the blocks likely encapsulate faults with slip rates high enough that they would separate blocks in better-studied regions. Regardless, for many if not most of the faults in central Tibet, this study provides the first late Quaternary to recent slip rate estimates, and it is hoped that they are valuable even if they are less well constrained than elsewhere.

4.4.1 Karakoram fault

The Karakoram fault is a well-known and well-studied ~1000 km long dextral fault that separates the northwestern Himalaya from western Tibet [Fig]. Like the Kunlun and Altyn Tagh faults, the Karakoram fault has been estimated to be slipping at a wide range of rates, and therefore to occupy different (but generally important) roles in various hypotheses for the geodynamics of Himalayan and Tibetan deformation (R. H. Styron et al., 2011).

The crust to either side of the Karakoram fault is broken into multiple blocks in the model, and consequently the slip rate on the Karakoram fault varies substantially along strike. The

northernmost Karakoram fault section separates the southeastern Pamir from extreme northwestern Tibet, and slips dextrally at $2.4 \pm 0.4 \text{ mm a}^{-1}$, with a very minor component of extension. However, south of the block boundary between the Pamir and the northwesternmost Himalaya, the strike-slip component decreases to $-0.5 \pm 0.4 \text{ mm/yr}$, while the fault system hosts $3.6 \pm 0.3 \text{ mm a}^{-1}$ of contraction; this is consistent with work by Robinson (2009) suggesting little to no late Quaternary strike-slip faulting on this section, and the contraction resolved on the fault zone may be linked to the extremely high peaks of the Karakoram range (including K2) adjacent to the fault. As postulated by Robinson (2009), dextral slip resumes farther southeast after the junction with the Longmu Co fault.

The central and southeastern Karakoram fault has dextral slip rates generally consistent at around 3 mm/yr ; these are slower than many of the geologic rates of about $2\text{--}8 \text{ mm/yr}$ (Brown, 2005; M.-L. Chevalier et al., 2005; M.-L. Chevalier et al., 2012; M.-L. Chevalier, Van der Woerd, et al., 2016) but do match the lowest of these.

4.4.2 Southern Tibetan rifts and dextral faults

Southern Tibet hosts a set of clearly-defined, regularly-spaced N-trending rifts that show clear kinematic linkages with ESE-striking dextral faults (e.g., Armijo et al., 1989). The dextral faults typically have conjugate NE-striking sinistral-normal faults (Taylor et al., 2003).

The westernmost of the rift and dextral fault systems is a pair of parallel, closely-spaced dextral faults that link with the Lunggar Rift [Kapp et al., 2008] and the Yari rift to the west. Each of these systems slips at about $1.5\text{--}3 \text{ mm a}^{-1}$ (varying along strike). These rates are consistent with geodetic work by Taylor & Peltzer (2006) and H. Wang et al. (2019) on the strike-slip faults, and extension rates over the Pliocene through present on the North Lunggar rift from thermochronology (Sundell et al., 2013), though this work predicts much slower rates than the Pliocene to present rates for the South Lunggar rift (R. H. Styron et al., 2013). These faults may be linked to the Lopukangri (Sanchez et al., 2013) and Xiagangjiang (Volkmer et al., 2007) rifts to the east, which show similar rates of extension.

The next system to the east is the Tangra Yum Co rift and linked Garze dextral fault, with respective extension and right-slip rates of $1.5 \pm 0.5 \text{ mm a}^{-1}$ and $0.9 \pm 0.5 \text{ mm a}^{-1}$. Notably, H. Wang et al. (2019) detected essentially no decadal strain accumulation across the Garze fault.

The Gyaring Co dextral fault and Pum Qu–Xainza rift lies further east, and is substantially faster than the neighboring rifts. The Gyaring Co fault, west of the junction with the Pum Qu–Xainza rift, shows $4.0 \pm 0.4 \text{ mm a}^{-1}$ of dextral slip, consistent with previous work (Shi et al., 2014; Taylor & Peltzer, 2006; H. Wang et al., 2019). The linked northern Pum Qu–Xainza rift extends at $2.0 \pm 0.5 \text{ mm a}^{-1}$, but the extension rate decreases to the south to near zero close to the northern Himalaya.

The central and northern Yadong–Gulu rift, including the Damxung and Nyainqntanghla grabens, extends at a similar rate as the other rifts ($\sim 0 \text{ mm a}^{-1}$), similar to geologic estimates (M.-L. Chevalier et al., 2020) but also has a consistent component of sinistral slip of $\sim 5 \text{ mm a}^{-1}$. Sinistral slip has long been recognized based on geologic evidence [REFS], though rates have remained geologically unquantified.

The easternmost rift, the Cona–Oiga Rift (e.g., Y. Wang et al., 2019) is less geomorphically developed than the other rifts (i.e., the rift basin is not as wide or continuous along strike, and the footwall is not as broad or as elevated above the basin), but has a rapid extension rate, about

6 mm a^{-1} . These rates are linked to the increase in eastward motion of Tibetan crust near the Eastern Himalayan Syntaxis and Eastern Tibet. Though the results estimated here are high, they are compatible with 3 Ma to present rates based on thermochronology of $1.6\text{--}3.8 \text{ mm a}^{-1}$ (Bian et al., 2020); these authors also suggest a late Pliocene initiation of extension, which may explain why the rift is not as developed as its neighbors to the west.

The Beng Co-Dong Co fault system is a small conjugate strike-slip system with some internal N-striking normal faults north of the Gulu Rift. The Beng Co fault, the southern, SE-striking, dextral fault is well known for hosting a very large ($M \approx 8$) earthquake in 1951. Early slip rate estimates are $10\text{--}20 \text{ mm a}^{-1}$ [Armijo et al., 1989; Wu et al., 1992], though more recent geologic and geodetic rates are $1\text{--}4 \text{ mm a}^{-1}$ (Garthwaite et al., 2013; Hollingsworth et al., 2010). Here, we estimate dextral slip rates of $0\text{--}1 \text{ mm a}^{-1}$, with a SE-ward increasing normal component. The conjugate sinistral fault to the north slips at $0.1\text{--}2 \text{ mm a}^{-1}$, with a small component of contraction. Combined extension across the Daru Co and Dong Co normal faults in between the strike-slip faults is about 3 mm a^{-1} , consistent with geologic rates (K. Li et al., 2019). However, all of these rates are informed by very few data, and localized studies or increased geodetic coverage could refine these values quite a bit.

The Jiali fault is mapped here with its western terminus where the southern end of the north-striking Gulu Rift meets the Damxung/ Nyainqntanghla rift. The Jiali Fault continues east, separating the southern Tibetan and Himalayan blocks from those of east-central Tibet, before splitting into several other faults north of the Eastern Himalayan Syntaxis. Though the Jiali fault has long been considered a dextral fault (e.g., Armijo et al., 1989), the western Jiali fault resolves as sinistral, similar to (and in continuation of) the northern Damxung rift, with sinistral slip of $1.6 \pm 0.3 \text{ mm a}^{-1}$. Though signs of Quaternary surface faulting are evident along the trace, no clear kinematic indicators were observed, and those noted by Armijo et al. (1989) were equivocal in the satellite imagery. The sinistral component decreases eastward, and the splaying faults to its east show rapid dextral slip (as discussed in Section 4.7.3).

consider moving to SE tibet The decrease in left slip rate on the Jiali fault is met by an increasing component of contraction across the fault zone, exceeding 1 cm/yr east of the Eastern Himalayan Syntaxis, where it is accommodated on two structures, the Puqu and Parlung faults. The terrain surrounding the eastern Jiali fault is high even by South Tibetan standards, with many peaks between 6-7 km, and the high-altitude areas are much more broad than the similarly high rift-flank uplifts farther west. This suggests that N-S contraction in the region may be somewhat distributed. Discrete active reverse faults have not been mapped to my knowledge, but the zone is easily among the world's most rugged and inaccessible.

4.4.3 Central Tibetan sinistral faults and associated normal faults

Central Tibet deforms through slip on NE-striking sinistral faults that are typically conjugates to dextral faults in southern Tibet (Taylor et al., 2003). These sinistral faults are commonly transtensile, with small extensional stepovers, rather than linking to large, well-defined rift systems as in southern Tibet.

The westernmost of these faults is the Longmu Co–Gozha Co fault system (Avouac & Tapponnier, 1993; M.-L. Chevalier et al., 2017), which links with the Yutian rift and Ashikule stepover (Bie & Ryder, 2014) before merging with the Altyn Tagh fault system (Section 4.5.2). This study finds that the Longmu Co fault (in the southwest) has a sinistral slip rate of $4.3 \pm 0.5 \text{ mm a}^{-1}$, in line with geologic estimates (M.-L. Chevalier et al., 2017), and the Gozha Co fault farther northeast

has a sinistral rate of $5.9 \pm 2.3 \text{ mm a}^{-1}$. The sinistral rate drops back down to $3.4 \pm 1.2 \text{ mm a}^{-1}$ with about 2 mm a^{-1} extension across the Yutian rift. This sinistral shear is transferred onto the Altyn Tagh fault to the northeast.

Spread over a thousand kilometers east of the Longmu Co–Gozha Co faults, several sets of E- to NE-striking sinistral faults (associated with minor NW- to NE-striking normal faults) accommodate E-W extension of Central Tibet. Almost all of them slip at about $2.5\text{--}3.5 \text{ mm a}^{-1}$, with some component of extension as well. The relative magnitudes of strike slip and extension vary substantially with fault strike (faults striking N or NW have the fastest extension and slowest strike-slip). The only Quaternary fault slip rate in the region is on a fault in the Shuang Hu graben; there, Blisniuk & Sharp (2003) find extension rates of about 0.1 mm a^{-1} on a single fault trace, which is a small fraction of the $5.9 \pm 1.3 \text{ mm/yr}$ extension found here across the entire rift at that location.

The longest and fastest-slipping of the NE-striking faults is a 450 km long fault called the Qixiang Co (or Kyebxian Co) fault, which is a conjugate of the Gyaring Co fault. The inversion here yields a sinistral slip rate of $4.2 \pm 0.6 \text{ mm a}^{-1}$, consistent with the Holocene rate of 3.6 ± 1.2 found by K. Li et al. (2018).

Generally, the blocks in north-central Tibet fan outward, with east-west extension increasing northward. The northern margin of this fan is the western Kunlun fault system, which acts here in a transfer capacity, increasing in slip rate to the east as extension between north-central Tibetan blocks is absorbed.

4.5 Northern Tibet

4.5.1 Kunlun fault system

The sinistral Kunlun fault system as mapped here extends for over 1500 km from northwestern Tibet east to near the Longmen Shan at the eastern margin of the orogen (Figure 7, 8). Like many of the major strike-slip systems in the orogen, the Kunlun fault system serves as a large-scale transfer fault (**fig Transfer**).

The westernmost part of this system has two parallel E-striking faults in this model; the southern fault is the Manyi fault, which ruptured in the eponymous $Mw 7.6$ event in 1997 (e.g., Funning et al., 2007), and the northern fault, which may be the western continuation of the Kunlun fault proper (Bell et al., 2011). The Manyi fault is at the northern terminus of the sinistral-normal faults of north-central Tibet; extension and sinistral slip to the south is transferred onto (or off of) sinistral slip on the Kunlun system. The western Manyi fault slips at $5.5 \pm 2.1 \text{ mm a}^{-1}$ sinistrally, increasing to 9.6 ± 1.8 past a junction with a rift system to the south.

Sinistral slip rates on the Kunlun fault increase to the east, as extension in north-central Tibet links in with the system. The west-central Kunlun fault slips at about $10.2 \pm 1.4 \text{ mm a}^{-1}$, increasing as reverse faults in the Qimen Tagh region to the north feed in. The highest rates are in the center of the fault system in the Dongdatan valley, at $8.9 \pm 0.4 \text{ mm a}^{-1}$ sinistrally, somewhat lower than Quaternary slip rates (J. Van der Woerd et al., 1998, 2001; J. V. der Van der Woerd et al., 2000). Slip rates on the Kunlun fault decrease by about half east of the center, as slip is transferred into the faults of the transpressional southeastern Qimen Tagh in northeastern Tibet and farther east from there (Mark B. Allen et al., 2017; e.g., Duvall & Clark, 2010). Sinistral slip rates on the eastern Kunlun fault are $3.4 \pm 0.3 \text{ mm a}^{-1}$, slightly below most Quaternary measurements (Harkins et al., 2010; e.g., Eric Kirby et al., 2007). Slip on the system remains significant towards

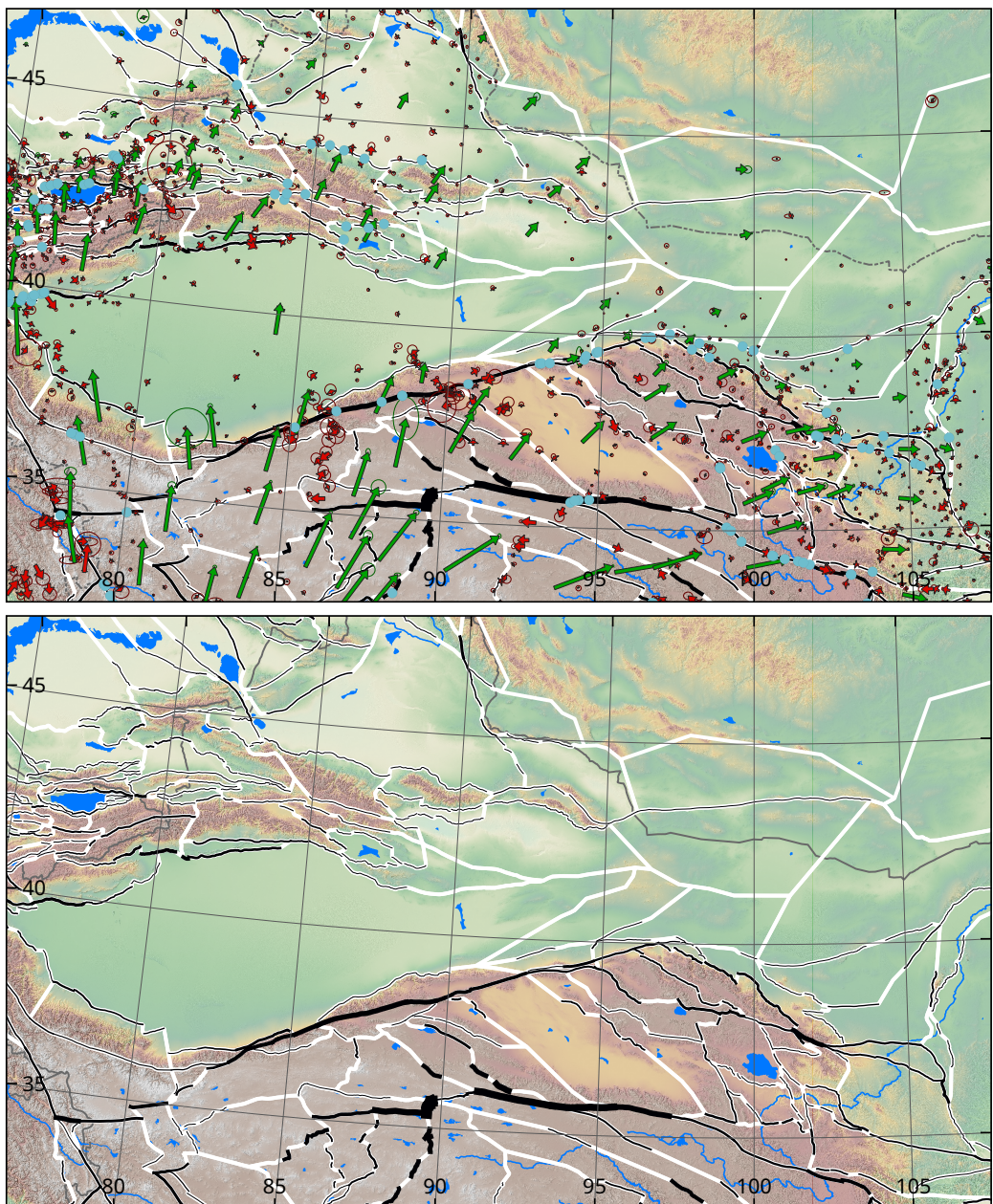


Figure 7: Northern Tibet

its eastern terminus, where it links with the faults of the Min Shan and Longmen Shan. The Kokoxili branch of the fault (which hosted the 2001 Mw 7.9 earthquake) slips at $3.0 \pm 0.4 \text{ mm a}^{-1}$ sinistrally.

4.5.2 Altyn Tagh fault system

The sinistral Altyn Tagh fault (Figure 7) is the longest strike-slip fault system in the Tibetan orogen (Figure 5). It is mapped continuously for 2000 km from the southeastern Pamir and along the northern rim of the Tibetan plateau just south of the Tarim Basin, until it [diminishes] at the northeasternmost thrusts of the Qilian Shan. It can be observed in satellite data discontinuously for another 800 km east to the northern Ordos block.

The Karakax fault is the westernmost fault in the Altyn Tagh system. The fault as mapped here has its northwestern end quite close to the Kongur Shan fault (Figure 4), and extends southeast for 500 km. Sinistral slip increases from $1.6 \pm 0.5 \text{ mm a}^{-1}$ in the northwest to $1.8 \pm 0.4 \text{ mm a}^{-1}$ farther east. There is very little extension or contraction across the fault zone; instead, contraction is accommodated on south-dipping thrust north of the Altyn Tagh where the Tarim basin underthrusts the Tibetan plateau. These thrusts show $1\text{--}2.5 \text{ mm a}^{-1}$ of contraction.

The northeast-striking Altyn Tagh fault proper begins where the Karakax fault and Longmu Co–Gozha Co faults join; the latter fault system has a much faster slip rate than the former, though the former has more structural continuity with the Altyn Tagh.

The fault system here is transpressional, with the Altyn Tagh fault trace flanked to the north and south by reverse faults, dipping towards the Altyn Tagh trace and uplifting narrow mountain ranges (e.g., Cowgill et al., 2000). However, the western Altyn Tagh fault zone itself seems to be transtensile, as evidenced by small releasing bends along its length. I find rates of sinistral slip on the western Altyn Tagh fault to be $5.7 \pm 0.9 \text{ mm a}^{-1}$, and $2.6 \pm 1.2 \text{ mm a}^{-1}$ extension. The oblique-reverse faults to the north and south of the primary Altyn Tagh trace accommodate a significant amount of the total deformation across the Altyn Tagh fault system as a whole, at least as expressed in the geodetic data, and compensate for the localized extension along the primary fault zone. These faults accommodate $0.9 \pm 1.0 \text{ mm a}^{-1}$ of left slip and $4.5 \pm 1.3 \text{ mm a}^{-1}$ shortening. The western Altyn Tagh fault system as a whole accommodates $6.6 \pm 1.2 \text{ mm a}^{-1}$ sinistral slip and $1.9 \pm 1.8 \text{ mm a}^{-1}$ shortening.

The central Altyn Tagh fault system also shows strain to be partitioned between the main Altyn Tagh fault, the North Altyn fault (Cowgill et al., 2000), and the Baiganghu fault to the south. Given the close proximity of these faults and the sparsity of the geodetic data, the block inversion cannot clearly differentiate strain accumulation rates on these three sub-parallel structures. Left unrestrained, the inversion allocates 2–3 mm/yr sinistral slip on each. Though no geologic rates have been published for the North Altyn and Baiganghu faults, sinistral slip of $\sim 3 \text{ mm/yr}$ is incompatible with geologic slip rates of $\sim 8.5\text{--}20 \text{ mm/yr}$ on the main Altyn Tagh trace. Therefore I have penalized slip rates on the splays. Following this, the main Altyn Tagh trace is found to slip here at $7.6 \pm 0.4 \text{ mm a}^{-1}$ sinistrally with little contraction; this is much more compatible, though still less than, the geologic slip rates of $\sim 8.5\text{--}9.5 \text{ mm a}^{-1}$ (e.g., Cowgill, 2007; Gold et al., 2009) at the well-studied Cherchen He and nearby sites, which use more realistic upper terrace ages for the reconstructions.

The Baiganghu fault (Liu et al., 2017), though essentially unstudied, displays very clear evidence for late Quaternary rupture in satellite imagery along its 160 km length. The Baiganghu fault shows $0.1 \pm 0.7 \text{ mm a}^{-1}$ of left-lateral slip and $-0.0 \pm 0.7 \text{ mm a}^{-1}$ extension in the southwest,

where it has a narrow mountain range with about 1 km relief in the footwall; both rates drop to near zero towards the northeast, after the junction with the thrusts of the Qimen Tagh, before it merges with the main Altyn Tagh fault.

Move to discussion It has been suggested that at least some of the discrepancy between the geologic and geodetic slip rate estimates of the Altyn Tagh relate to the long duration between the instrumental time and the most recent large earthquake (Hilley et al., 2009; K. Wang et al., 2021). Viscoelastic theory predicts that strain rates across a fault should be much higher relatively soon after large earthquakes as the lower crust and upper mantle flow to reduce coseismic stress concentrations, while at longer timeframes, closer to or exceeding the mean recurrence interval for large earthquakes, strain rates across the fault may be much less than the long-term rate (Hetland & Hager, 2005). The most recent large event on the Xorkol segment of the Altyn Tagh fault was approximately 1598, and that segment has a mean recurrence interval of 620 ± 410 years (Z. Yuan et al., 2018), indicating that the fault here is somewhat late in the earthquake cycle. The segment to the west, where some of the most robust geologic slip rate estimates have been made (Cowgill, 2007; Gold et al., 2009), and where the geologic-geodetic misfits are highest, has not been investigated paleoseismically, so it is unknown where in the earthquake cycle that segment fault is. Additionally, Dolan & Meade (2017) have found that these predictions from viscoelastic theory have not been consistently met by comparisons of geologic slip rates with geodetic slip rates from before and after large strike-slip earthquakes.

The slip rate on the Altyn Tagh fault system decreases to the northeast, as slip is transferred into NW-striking thrust faults of the Qilian Shan–Nan Shan ranges (e.g., Meyer et al., 1998; Yin et al., 2008). The Xorkoli segment of the Altyn Tagh is east of the junction with the Qimen Tagh ranges, with a sinistral rate of $5.5 \pm 0.3 \text{ mm a}^{-1}$. At the Akato Bend, the fault splits into two branches. The southern branch loses much of its rate to the east before joining with the thrusts of the western Qilian Shan, while the northern branch increases its rate to the east; the rates estimated here are in reasonable agreement with Elliott et al. (2018). Farther to the northeast, the fault slips sinistrally at $2.9 \pm 1.0 \text{ mm a}^{-1}$, progressively losing slip to the Qilian Shan thrusts until the Hexi Corridor (Figure 8).

4.5.3 Gobi-Altai and Gobi

The Gobi-Altai region lies at the intersection of Mongolia, Kazakhstan, China and Russia (Figure 7). The region has experienced some of the largest intraplate earthquakes in recorded history, (e.g., Chéry et al., 2001; Schlupp & Cisternas, 2007) along distributed strike-slip faults. The fault network is continuous with faults in the northeastern and southeastern Tien Shan [Section 4.1] and extends east through Mongolia and the Baikal region of Russia. Only faults on the southern and western margins of the region are included in this study; a fault dataset covering Northeastern Asia (R. Styron et al., 2018) has been produced by GEM as part of a seismic hazard model, though no block modeling has been completed for that dataset.

Deformation in the western Gobi-Altai is transpressive; east-striking structures accommodate N-S contraction (up to $\sim 2.5 \text{ mm a}^{-1}$) with a secondary sinistral component, while NW-striking structures are dextral-reverse with similar rates; most prominent in this latter set is the Fu-Yun fault that produced a $M 7.9$ earthquake in 1931 (Klinger et al., 2011; Tapponnier & Molnar, 1979), with $2.6 \pm 0.9 \text{ mm a}^{-1}$ dextral and $1.8 \pm 0.5 \text{ mm a}^{-1}$ contraction.

To the southeast, the faults of the Tien Shan continue east, with decreasing slip rates. Contraction across the far eastern Tien Shan around the Turfan Depression is $0.7 \pm 0.7 \text{ mm a}^{-1}$, somewhat

faster than Quaternary rates by Charreau et al. (2017). The 700 km long master fault of the Gobi–Tien Shan Fault System (e.g., Cunningham, 2013) shows a left-reverse slip rate of $1.2 \pm 2.1 \text{ mm a}^{-1}$.

4.5.4 Qimen Tagh

The Qimen Tagh comprises several closely-spaced mountain ranges extending from the central Altyn Tagh fault, east of the Cherchen He site, to the central Kunlun fault (Figure 8). The ranges are sinistral-reverse, with slip rates that increase towards the south. The Ayak Kum Kol thrust in the north shows $-1.9 \pm 0.8 \text{ mm a}^{-1}$ sinistral and $3.9 \pm 1.2 \text{ mm a}^{-1}$ reverse rates, while the Narin thrust along strike to the southeast shows $-0.9 \pm 0.8 \text{ mm a}^{-1}$ and $9.9 \pm 2.8 \text{ mm a}^{-1}$ sinistral and reverse slip, respectively. Like the Qilian Shan thrust belt farther east, these thrusts form a very large transpressional stepover between the Altyn Tagh and Kunlun faults, essentially transferring sinistral slip from the western Altyn Tagh to the central Kunlun.

4.5.5 Qilian Shan and Hexi Corridor

The Qilian Shan is a contractional basin and range zone that is the northeastern limit of the high topography of the Tibetan orogen. The region hosts an array of NW-striking reverse faults, and WNW- and NNW-striking strike-slip faults. The reverse faults of the Qilian Shan have contractional rates between $1.8\text{--}4 \text{ mm a}^{-1}$, with up to 3 mm a^{-1} sinistral slip. The northeastern Altyn Tagh fault borders the Qilian Shan on the northwestern margin, and a substantial decrease in its slip rate is linked to crustal shortening along the Qilian Shan, particularly the northeasternmost (frontal) Qilian Shan thrust along the Hexi Corridor. Shortening of this latter structure is $4.2 \pm 0.5 \text{ mm a}^{-1}$ in this study, far greater than geologic slip rates (W. Chen, 2003; W. Min et al., 2002).

The Haiyuan fault is a $\sim 1000 \text{ km}$ long WNW-striking sinistral fault that bisects the Qilian Shan. It is well studied in part because of a great ($M 8+$) earthquake in 1920 (e.g., Liu-Zeng et al., 2007). Like many of the strike-slip faults in the orogen, the slip rate on the Haiyuan fault system is highest in its central segments [Figure 5], increasing from $2.1 \pm 0.9 \text{ mm a}^{-1}$ in the west to $5.7 \pm 0.3 \text{ mm a}^{-1}$ in the central (Lenglongling) segment, as the Qilian Shan thrust feeds slip in. To the east, it splits, with the northern branch becoming the Tianjingshan fault and the southern continuing as the Haiyuan. The central and eastern Haiyuan and the Tianjinshan faults have received substantial geologic investigation. The rates here are consistent with modern studies (Jiang et al., 2017; C. Li et al., 2009; X. Li et al., 2017; Zheng et al., 2013) although the geologic studies predict slightly higher slip rates on the eastern Haiyuan and lower rates on the Tianjinshan to the north.

South of the Haiyuan fault, the WNW-trending ranges are cut by two prominent NW-striking dextral faults that extend south to near the Kunlun fault, the Riyueshan and Elashan faults. These faults accommodate NE-SW shortening and distributed sinistral shear through counterclockwise bookshelf rotation (Duvall & Clark, 2010). Dextral rates on each fault are $3\text{--}2 \text{ mm a}^{-1}$, in line with geologic estimates (D.-Y. Yuan et al., 2011).

The Qinling fault parallels the Haiyuan fault about 200 km south of the Haiyuan, extending farther east into the Weihe graben, which separates the Ordos block in the north from the Qinling mountains to the south. The western

- weihe graben Rao et al. (2014) $2\text{--}5 \text{ mm a}^{-1}$ dip lip, cant locate

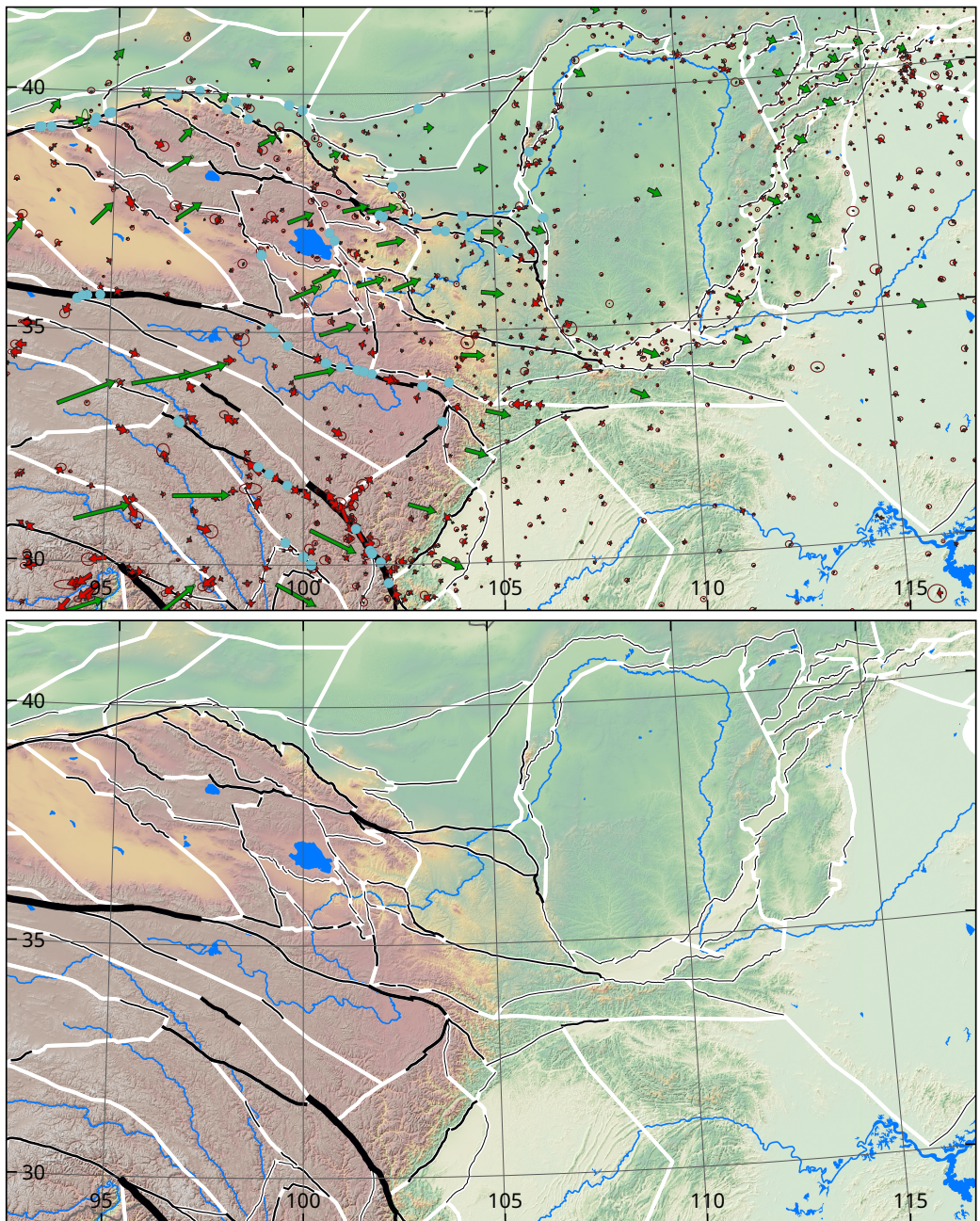


Figure 8: Northeastern Tibet

4.6 Eastern Tibet and the Longmen Shan

The eastern margin of the Tibetan plateau is a physiographic and kinematic transition zone. Here, the rapid strain rates and structural complexity of the high orogen grade into much slower (and less dense) fault separating larger blocks of eastern China. However, the fault slip rates are still moderate by global standards. Most are above the global median of 0.6 mm a^{-1} for intraplate faults (R. Styron & Pagani, 2020). Combined with the dramatic increase in population density at the orogenic front (from around XX /km² in the plateau interior to YY/km² in the Sichuan Basin), this region has some of the highest seismic risk in China.

4.6.1 Eastern termination of the Kunlun fault

Though the slip rate of the Kunlun fault decreases eastward from its central high [Figure 5; Section ??], this study shows that the rate increases at its eastern terminus, where the Bayan Har crust south of the fault moves rapidly east against the relatively slower western Qinling crust. At this point, the easternmost Kunlun fault (the Maqu segment (Lin & Guo, 2008)) splits into the parallel Bailongjiang fault to the northeast and the Tazang fault to the southeast. Though geologic sinistral slip rates on each branch are around 2 mm a^{-1} (H. Li et al., 2020; Ren et al., 2013b), this study finds equivalent rates for the Bailongjiang but faster rates of $5.6 \pm 0.3 \text{ mm a}^{-1}$ for the Tazang.

4.6.2 Longmen Shan

The eastern Tazang fault meets three faults in the Min Shan region. The Longriba fault (Ren et al., 2013a; XiWei Xu et al., 2008) to the southwest is the fastest slipping, with $4.3 \pm 0.4 \text{ mm a}^{-1}$ right-lateral slip and $3.3 \pm 0.5 \text{ mm a}^{-1}$ shortening. These rates decrease following the block boundary to the southwest, past where the Longriba fault has been mapped or is readily identifiable in satellite imagery. The middle fault east of this fault junction is the Min Shan fault (E. Kirby et al., 2000), and the easternmost may be unnamed; these two faults have sinistral-reverse slip rates of $1\text{--}3 \text{ mm a}^{-1}$.

The southeastern margin of the Longmenshan is bounded by the Longmenshan fault zone, most well known for the devastating 2008 M 7.9 Wenchuan earthquake. The results here show that the Longmenshan rangefront fault (here representing both the Beichuan and Pengguan faults (Densmore et al., 2007), though located at the Pengguan fault trace) has $1.4 \pm 0.3 \text{ mm a}^{-1}$ contraction and $3.6 \pm 0.4 \text{ mm a}^{-1}$ dextral slip, which change along strike to the northeast to $3.7 \pm 0.3 \text{ mm a}^{-1}$ dextral and $1.4 \pm 0.4 \text{ mm a}^{-1}$. This northeastern decrease in contraction and increase in dextral shear was also seen in the kinematics of the 2008 earthquake rupture (Xiwei Xu et al., 2009; Zhang et al., 2011).

We also find just over $1.0 \pm 0.2 \text{ mm a}^{-1}$ left-reverse slip on the Longquan fault in western Sichuan Basin.

4.6.3 Tanggula Shan and unexplored region

4.6.4 Xianshuihe–Xiaojiang fault system

South of the eastern Kunlun fault, the sinistral Xianshuihe–Xiaojiang fault system (XXF) is another great strike-slip fault system in the orogen. Like the Altyn Tagh, Kunlun, and Haiyuan fault systems, the XXF accommodates (south)eastward transport of Tibetan crust away from the

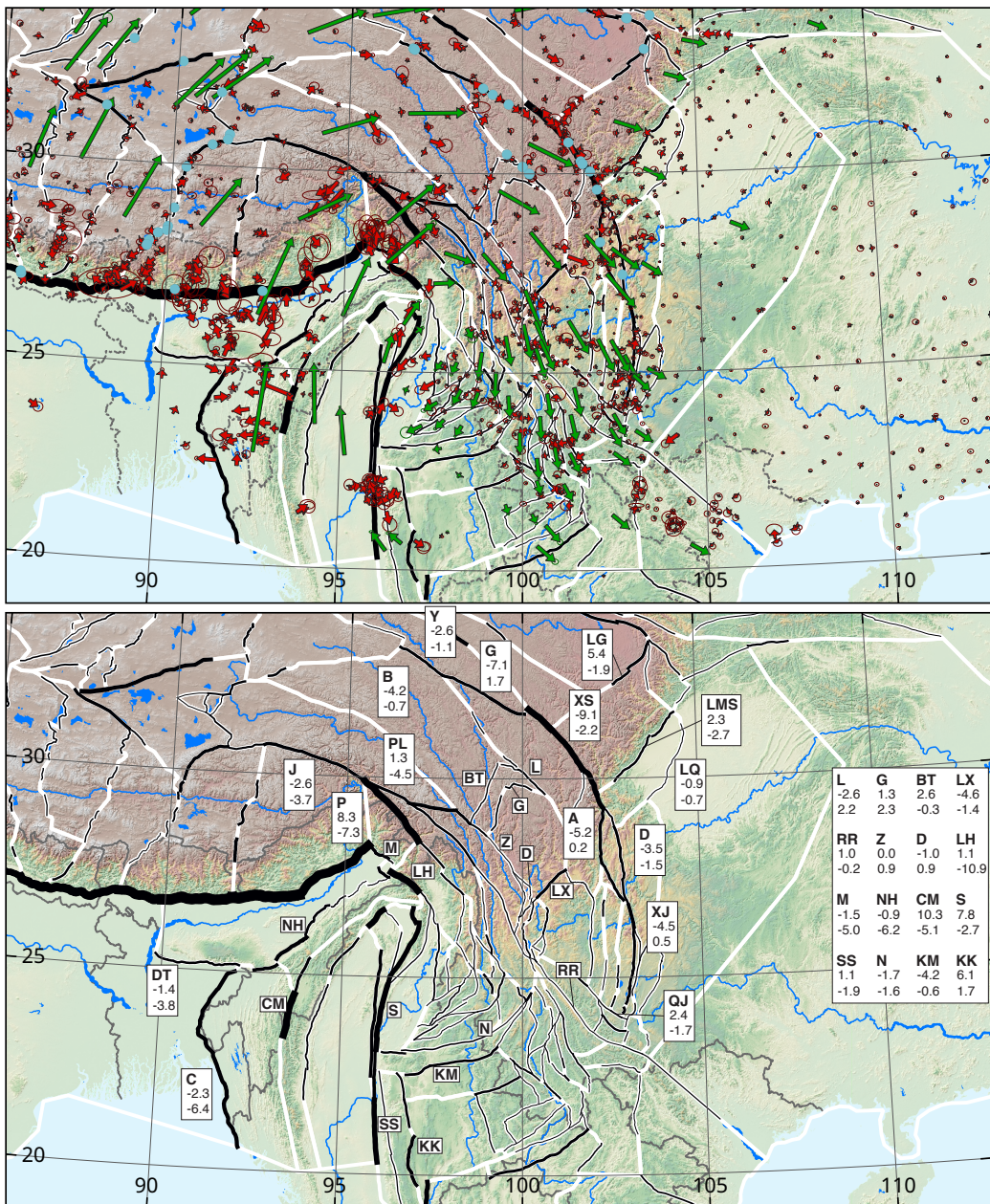


Figure 9: Southeastern Tibet. Y = Yushu fault. B = Batang fault. G = Garze fault. XS = Xianshuihe fault. A = Anninghe fault. D = Daliangshan fault. XJ = Xiaojiang fault.

impinging Indian crust (e.g., Peltzer & Tapponnier, 1988). Unlike the others, however, the XXF is arcuate, approximating a small circle around the Eastern Himalaya Syntaxis, and is paired by parallel (rather than conjugate) dextral faults, the Jiali and Sagaing fault systems [Figure 1]. The crust in between the fault systems moves south-southeast with more gentle internal velocity (and topography) gradients compared to the gradients across the bounding faults; its motion has been referred to as “channel flow”

The XXF starts in the NE along the Jinsha suture [yang et al 2012 tectonics]. Here, the fault system comprises several en-echelon segments, including the Yushu segment which ruptured in 2010 (e.g., Z. Li et al., 2011), and a splay fault called the Batang fault. Geologic left-lateral slip rates for the Yushu segment are around 7.5 mm a^{-1} , and another 3 mm a^{-1} for the Batang fault (Huang et al., 2019). This work yields sinistral rates of 2.6 mm a^{-1} for the Yushu and 4.2 mm a^{-1} for the Batang fault, with a rate of 7 mm a^{-1} for the segment immediately SE of the Yushu–Batang junction. The equivalence between the geologic slip rates northwest of the junction with the block rates southeast of the junction suggests that a modified block geometry would be able to match the geologic data for the Yushu segment quite well; however, it is not possible to modify the geometry here without removing the Batang fault from the model.

Southeast of this junction, however, the block model matches the geologic slip rate estimates much more closely. Sinistral rates vary between $5\text{--}9 \text{ mm a}^{-1}$, generally increasing SE, capturing local variations in geologic rates (Bai et al., 2018; G. Chen et al., 2016; M.-L. Chevalier et al., 2018), with the exception of a rather high rate of 17 mm a^{-1} using a lower terrace age by G. Chen et al. (2016). The variation between $5\text{--}9 \text{ mm a}^{-1}$ is related both to changes in fault strike relative to the regional velocity field, and to the branching or merging of secondary faults with the XXF and the consequent changes of relative block motion along strike. Much of these along-strike changes in sinistral slip rate are linked to changes in convergence across the fault zone as well; for example, a decrease in

Fault branches are more common on the southeastern XXF than the northwest. The most prominent is a branch at the southeastern Xianshuihe fault, where it splits into the Anninghe fault to the southwest and the Daliangshan fault to the southeast. The Anninghe fault takes more than half of the southern Xianshuihe fault, $5.8 \pm 0.4 \text{ mm a}^{-1}$ (He & Ikeda, 2007), while the Daliangshan fault takes $4.8 \pm 0.4 \text{ mm a}^{-1}$ (He et al., 2008). These faults merge about 275 km south of the northern split, at the northern Xiaojiang fault.

The Xiaojiang fault runs N-S for about 300 km through eastern Yunnan province. In the north, the slip rate is just over $7.1 \pm 0.4 \text{ mm a}^{-1}$, decreasing slightly to the south. The Xiaojiang fault is the fastest slipping, and perhaps most clearly defined, of 5–6 parallel sinistral faults spaced 10–40 km apart. The next fault to the west, the Puduhe fault, runs through Kunming (the capital of Yunnan, with a metro area population above 6 million), has a sinistral rate of $1.7 \pm 0.3 \text{ mm a}^{-1}$. These faults accommodate $>10 \text{ mm a}^{-1}$ sinistral shear. All of these faults terminate to the south against the Qujiang fault, a dextral splay of the Red River fault.

4.7 Southeastern Tibet and Indochina

In contrast to most of the margins of the Tibetan plateau, the southeastern margin is topographically gentle (Clark & Royden, 2000) and has a similarly broad and gentle velocity gradient with respect to south China (Gan et al., 2007), which is not accommodated by reverse faulting. The region can be roughly characterized by a clockwise rotation of a package of crustal material around the Eastern Himalayan Syntaxis, bound on the outer (northern and eastern) margins by

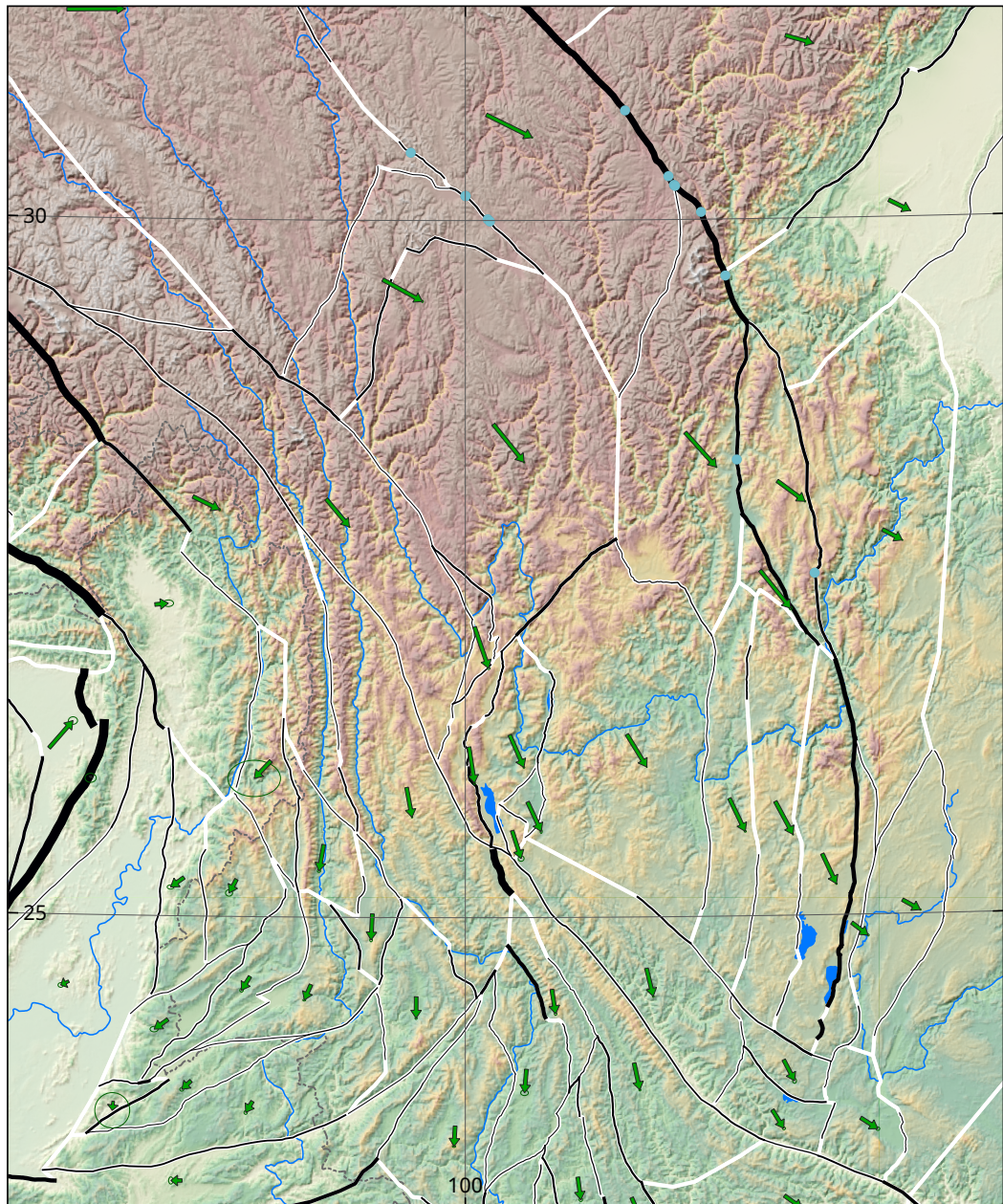


Figure 10: Hengduan area

the XXF and on the inner by the Puqu and Sagaing faults systems. However, some second-order patterns are important, as well: First, this rotating package of crust is cut obliquely by the dextral Red River fault system, which marks a distinct change in the configuration of faults and blocks on either side, and leads to some structural complexities such as fault stepovers. Second, this rotating package of crust is also undergoing sinistral shear along concentric planes, such that the inner parts of the package have a greater angular velocity than the outer parts; this is particularly apparent southeast of the Red River fault system. All of these factors lead to greater tectonic complexity than is found anywhere else in the orogen.

In spite of the tectonic complexity, the area has received comparatively little neotectonic study. GNSS coverage is good within China and northern Viet Nam, but is very sparse in Burma, Laos, and northern Thailand. Very little geologic slip rate data is available, and none were found south of the Red River fault. While this made characterizing and modeling the region more challenging than some other regions, it also means that there is a great opportunity for future work, which will refine or refute the results presented here.

4.7.1 High-elevation transtensional faults

The high plateau margin in between the Longmen Shan and the Eastern Himalayan Syntaxis, often called the Hengduan Shan, has relatively few known faults. The few that are known are transtensional, indicating that the crust is accelerating to the SE here. The most well-studied fault is the Litang fault, a sinistral-normal fault parallel to the Xianshuihe fault; the sinistral slip rate on this fault 2.6 ± 0.3 to 3.6 ± 0.5 along strike to the SE, and changes from slightly contractional to having a larger normal component, in reasonable agreement with late Quaternary rates (M.-L. Chevalier, Leloup, et al., 2016; Xiwei Xu et al., 2005).

The Litang fault and its splays are paired by two NE-striking conjugate right-lateral faults, which terminate to the southwest against the Zhongdian fault. The longer, western fault is the Batang fault (E. Wang & Burchfiel, 2000) (not to be confused with another Batang fault at the northwestern end of the XXF), with 1.2 ± 0.5 mm a⁻¹ dextral slip. The eastern fault is not previously described to my knowledge, but has an 85 km long, straight fault trace that is well expressed in topographic and satellite imagery. Most interestingly, this fault is interpreted to meet its conjugate left-normal fault at a narrow Quaternary basin at the foot of the 6200 m Ge'Nyen peak. The mountain front of this peak rises 2600 m above the basin and has well-developed triangular facets up to 1 km tall. This morphology strongly suggests that the peak is the footwall of a relatively narrow rift, an interpretation supported by several moderate magnitude normal earthquakes in 1989 with compatible focal mechanisms. The block model results place 2.3 ± 0.4 mm a⁻¹ extension on this fault.

4.7.2 Zhongdian–Lijiang–Dali fault system

Another zone of structural complexity exists in northern Yunnan and southwestern Sichuan provinces, south of the transtensional faults mentioned in Section 4.7.1 (Figure 9). The Zhongdian fault is a dextral fault that parallels the northernmost Red River fault about 80 km northeast of the latter fault. At its southwestern end, it splays into a set of transtensional faults that function as a broad extensional stepover between the Zhondian and central Red River faults. This zone stretches from Tiger Leaping Gorge just north of Lijiang, south to Dali where the system meets the Red River fault. The Lijiang–Xiaojinhe fault (Xiwei Xu et al., 2003) extends from this area northeast to a half-graben near Yanjingzhen, breaking up the 500 km in between the Litang and

Red River splays into two blocks.

At Tiger Leaping Gorge, the Daju normal fault raises the Jade Dragon Snow Mountain in its footwall, creating the 3800 m deep gorge. I find extension of about 3.2 ± 0.9 mm/yr on this fault, in agreement with the 4 mm/yr rate observed through dating of the fault scarp by Kong et al. (2010). South of the intersection with the Lijiang–Xiaojinhe fault, the north-striking faults in the Lijiang and Dali areas accommodate about 5 mm/yr of E-W extension, with lower sinistral strike-slip rates that vary locally based on local block rotations. The Lijiang–Xiaojinhe fault itself accommodates 4.8 ± 0.5 mm/yr left-slip, with a subordinate reverse component, similar to geologic rates estimated by Xiwei Xu et al. (2003).

4.7.3 Red River fault system

At the Eastern Himalayan Syntaxis, the Jiali fault splits into the dextral-reverse Parlung and Puqu faults. The Parlung fault continues southeast to the South China Sea as the Red River fault system, while the Puqu fault feeds dextral slip south into a complicated stepover system in northernmost Myanmar that eventually merges with the Sagaing fault system.

Both the Parlung and Puqu faults absorb a substantial amount of shortening (over 10 mm a^{-1} between them). The area in between the faults is the Kangri Garpo range, which tops out above 6800 m, though the Puqu fault itself is at elevations as low as 1400 m where it crosses the Chayu (Lohit) river a short distance from the range crest. The locations of the Puqu and Parlung faults are readily apparent based on the linearity of the river valleys superposed on them, and separate major tectonostratigraphic packages (Ding et al., 2001), though the active traces are not easily observed in topographic and satellite imagery. Nonetheless, given the linearity of the inferred traces across several kilometers of relief, the faults must dip fairly steeply, so the shortening across the fault systems is likely accommodated on auxiliary reverse faults and perhaps crustal folding. Alternatively, it is possible that the true fault surface of the megathrust as it wraps around from the NW-dipping Main Himalayan Thrust system of the eastermost Himalaya to the NE-dipping Mishmi Thrust is poorly represented by the rectangular faults in the block model, and that much of this shortening is actually accommodated on the Mishmi Thrust (Section 4.7.4).

The Puqu fault also has a high dextral slip rate. The northwestern section of the fault slips dextrally at 6.1 ± 0.9 mm a^{-1} , though this rate decreases dramatically to the southeast. The concern with this rate is the same as with the convergence rate noted previously.

The Red River fault extends southeast from the Parlung fault, cutting through the clockwise rotating crust of Southeast Tibet with a dextral slip rate varying between 0.1 – 3 mm a^{-1} . Sinistral fault systems to the northeast and southwest terminate against the Red River fault, rather than offsetting it (C. R. Allen et al., 1984). However the clockwise rotation does seem to deform the Red River fault (e.g., Schoenbohm et al., 2006). The trace of the fault is offset in map pattern by about 60 km to the southwest over the central 650 km of the whole trace; the location of this deflection corresponds to the most rapid clockwise rotation, from west of Lijiang to the intersection with the Xiaojiang fault system. The fault-normal component of deformation at the bends is opposite to that of typical releasing and restraining bends. A retrodeformation of the block model using the instantaneous Euler poles derived in this study shows that the Red River fault system would be approximately linear at about 5–6 Ma, which suggests that may have been linear in the past (I do not think this should be taken for granted, and I do not think *a priori* that the Euler poles derived here apply millions of years in the past, so the 5–6 Ma age may not be particularly meaningful). Of the major strike-slip fault systems in Tibet, the Red River fault

is the only one that deforms in such a manner; it may be a rare phenomenon worldwide, and indicative of unique or superposed tectonic conditions.

4.7.4 Northeast Assam and Mishmi thrust

The northeastern margin of the Assam valley is bordered by the Mishmi hills which rise progressively into the Kangri Garpo range. These mountains are underlain by the Mishmi thrust, the source of the 1950 Mw ~ 8.6 Assam earthquake (Priyanka et al., 2017). I find contraction rates of 6.7 ± 0.7 mm a $^{-1}$ across the Mishmi thrust, with minor strike-slip motion. This rate is fairly high by most standards but one third to one half of the contraction across the adjacent Main Himalaya Thrust. It is also substantially lower than the along-strike continuation to the south, where the northeastern Indo-Burman ranges converge with the crust of northernmost Myanmar along the Dihing River.

4.7.5 Clockwise rotation and sinistral shear in Myanmar and Yunnan

West of the northern Red River fault system and the Lijiang–Dali area, deformation is accommodated through dextral shear along N-striking strike-slip faults in the valleys of the Nu (Mekong) and Lancang (Salween) rivers; these faults are the northern part of the regionally-important Cenozoic Gaoligong dextral shear zone (G. Wang et al., 2008). Dextral slip across these faults is cumulatively about 5 mm/yr. The system changes dramatically from transpressive in the north (related to Himalayan convergence) to transtensile in the south (potentially linked to toroidal mantle flow around the Eastern Himalayan Syntaxis (Soto et al., 2012)).

South of the north-striking dextral faults of the northern Gaoligong shear zone, deformation in eastern Myanmar and western Yunnan is primarily accommodated by arcuate, E– to NE-striking sinistral faults that describe small circles around the Eastern Himalaya Syntaxis (similar to the XXF). The northernmost of these faults are relatively short and linked to the north-striking dextral faults; these faults are part of the southwestern Gaoligong shear zone (G. Wang et al., 2008). South of this shear zone, the arcuate sinistral faults become much longer (300–500 km) and in some cases extend from the Sagaing fault to the Red River fault. In other cases, the fault and block geometry is more complex, particularly where E–W extension is more rapid. The most clear case of this is south of the eastern Nanting fault (the longest of the E–W faults), where the crustal velocity field diverges; to the northwest, the GNSS stations move southwest with respect to Eurasia (part of the clockwise rotation), but to the southeast, the GNSS stations move south and then southeast (a counterclockwise rotation). The smaller blocks west of the Red River fault and south of the Nanting fault accommodate the divergence in the velocity field through counterclockwise bookshelf rotation, with dextral and extensional slip on the faults between them.

farther south

more E-striking left-slip

velocity dissipation, N-S regional shortening and E-W regional extension on conjugate SS faults

4.7.6 Sagaing fault

The north–striking dextral Sagaing fault is directly south of the Eastern Himalaya Syntaxis, running from the Indo-Burman ranges of northern Myanmar south to the Indian Ocean at the

Irrawaddy delta. The Sagaing fault is generally considered the main plate boundary fault between the Indian and Eurasian (or Indochina) plates southeast of the Himalaya (Vigny et al., 2003).

Though the total velocity difference between the crust on either side of the Sagaing fault system is about 15 mm a^{-1} , the block model suggests that this is accommodated both by fault slip and block rotation. The northern Sagaing fault (between 23°N and 25°N latitude) is split into two strands, with 3.9 ± 1.6 and $16.0 \pm 1.9 \text{ mm/yr}$ dextral slip in the west and east, respectively. Between 23°N and 20°N , the Sagaing is single-stranded, with $10.6 \pm 1.6 \text{ mm/yr}$ of dextral slip, but closely paralleled to the east by the Shan Scarp fault (with $5.2 \pm 1.4 \text{ mm a}^{-1}$ dextral slip), and the Kyaukkyan fault (S. Min et al., 2017) another 65 km to the east, with $4.1 \pm 1.8 \text{ mm a}^{-1}$ dextral shear. Dip slip is variable but minor on these structures.

The northernmost portion of the Sagaing fault system

4.7.7 Indo-Burman ranges and the Shillong Plateau

The Shillong Plateau is a basement-cored pop-up

The Dauki fault on the south side of the Shillong Plateau accommodates $4.1 \pm 0.4 \text{ mm a}^{-1}$ of reverse-sinistral slip.

The Indo-Burman ranges form a N–to NW-striking thrust belt between the Indian subcontinent and the crust of southeastern Eurasia and Indochina, west of the Sagaing fault. The Indo-Burman ranges accommodate contraction related to the eastward component of India’s motion relative to Myanmar, as well as some dextral shear on north-striking faults.

The Indo-Burman ranges can be divided into two segments that are partially separated by the eastern Shillong Plateau. The Naga Hills are in the northeast, where the ranges overthrust the Indian crust in the Brahmaputra valley, opposite the easternmost Himalaya. The Chittagong-Tripura fold belt, a thrust wedge atop the east-dipping Chittagong Coastal Thrust, occupies the southwestern part of the ranges. The north-striking Churachandpur Mao fault forms the backstop to the thrust wedge here.

The Chittagong Coastal thrust accommodates much of the E–W shortening across the Indo-Burman ranges south of the Naga Hills. Contraction ranges from $7.5 \pm 1.0 \text{ mm a}^{-1}$ in the south to 0.4 ± 0.4 in the north. Early block model geometries of this region had a single block for the entire fold belt west of the Churachandpur Mao fault, but patterns in the residual GNSS velocities indicated that shortening was occurring within the wedge. An additional N-striking thrust was added, cutting the fold belt in twain, somewhat arbitrarily at a boundary between relatively widely-spaced, low-elevation faults and folds to the west and more tightly-spaced, higher-elevation structures to the east. This removes the systematic pattern to the residuals. Unlike the Chittagong Coastal Thrust, contraction across this fault is highest in the north at $4.0 \pm 0.6 \text{ mm a}^{-1}$, decreasing to near zero towards the coast where more shortening is accommodated on the western frontal thrust.

The Naga Hills thrust shows $4.5 \pm 1.5 \text{ mm a}^{-1}$ contraction near the midpoint of the range, with rates increasing from northeast to southwest, consistent with a clockwise rotation of the block [e.g., vernant]. A dextral component is resolved as well, though this varies with variations in strike.

The model results for the southeastern side of the Naga Hills and the junctures with Kapaw and Sagaing fault systems run against the typical structural interpretation of the region, with

contractional structures (reverse faults and folds) between the Naga Hills and the crust to the south [refs], which are readily observed in satellite imagery. In contrast, the model results show fairly rapid N–S extension between the Naga Hills and the crust to the south; this extension is faster than the convergence between the Naga Hills and Assam. This is clearly visible in the geodetic velocities, as the GNSS stations in the Naga Hills move to the north much faster (about 10 mm a^{-1}) than those to the southeast. However, the data only exist in the southwestern part of the Naga Hills. Given that the velocity vectors in Assam, the Naga Hills and the basins to the south are close to parallel, it is possible that the velocity gradients can be accommodated through dextral shear on faults parallel to the velocities, although no suitable structures have been mapped or may be inferred from the topography. Rapid orocinal bending of the Naga Hills block may also resolve this discrepancy.

4.8 Eastern and Northeastern China

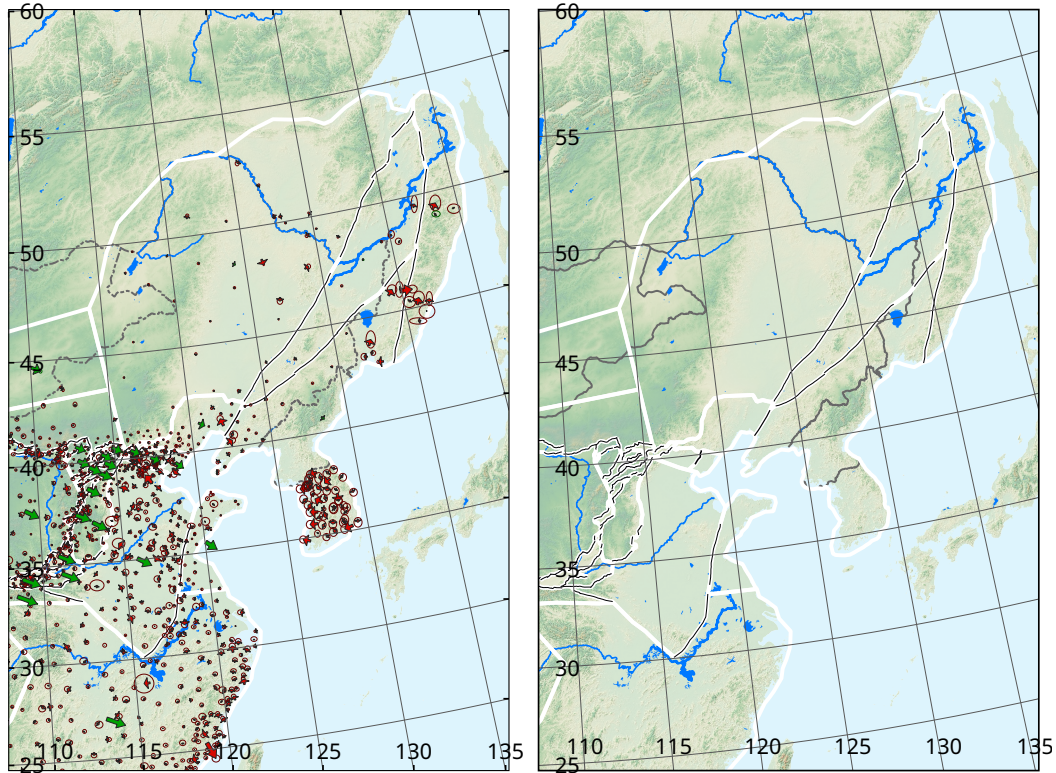


Figure 11: Northeastern China

- 4.8.1 Shaanxi graben area
- 4.8.2 Yitang-Yilong fault, Tanlu fault
- 4.8.3 Tianjin and Bohai Sea

5 Discussion

5.1 Comparison of

6 Conclusions

References

- Abdel-Aziz, M. R. (2006). On the solution of constrained and weighted linear least squares problems. *International Mathematical Forum*, 1067–1076. <https://doi.org/10.12988/imf.2006.06087>
- Ader, T., Avouac, J.-P., Liu-Zeng, J., Lyon-Caen, H., Bollinger, L., Galetzka, J., et al. (2012). Convergence rate across the Nepal Himalaya and interseismic coupling on the Main Himalayan Thrust: Implications for seismic hazard. *Journal of Geophysical Research: Solid Earth*, 117(B4), n/a–n/a. <https://doi.org/10.1029/2011JB009071>
- Allen, C. R., Gillespie, A. R., Han, Y., Sieh, K. E., Zhang, B., & Zhu, C. (1984). Red River and associated faults, Yunnan Province, China: Quaternary geology, slip rates, and seismic hazard. *GSA Bulletin*, 95(6), 686–700. [https://doi.org/10.1130/0016-7606\(1984\)95%3C686:RRAAFY%3E2.0.CO;2](https://doi.org/10.1130/0016-7606(1984)95%3C686:RRAAFY%3E2.0.CO;2)
- Allen, M. B., Alsop, G. I., & Zhemchuzhnikov, V. G. (2001). Dome and basin refolding and transpressive inversion along the Karatau Fault System, southern Kazakhstan. *Journal of the Geological Society*, 158(1), 83–95. <https://doi.org/10.1144/jgs.158.1.83>
- Allen, Mark B., Walters, R. J., Song, S., Saville, C., Paola, N. D., Ford, J., et al. (2017). Partitioning of oblique convergence coupled to the fault locking behavior of fold-and-thrust belts: Evidence from the Qilian Shan, northeastern Tibetan Plateau. *Tectonics*, 36(9), 1679–1698. <https://doi.org/10.1002/2017TC004476>
- Armijo, R., Tapponnier, P., Mercier, J. L., & Han, T.-L. (1986). Quaternary extension in southern Tibet: Field observations and tectonic implications. *Journal of Geophysical Research*, 91(B14), 13803. <https://doi.org/10.1029/JB091iB14p13803>
- Armijo, R., Tapponnier, P., & Han, T. (1989). Late Cenozoic right-lateral strike-slip faulting in southern Tibet. *Journal of Geophysical Research: Solid Earth*, 94(B3), 2787–2838. <https://doi.org/https://doi.org/10.1029/JB094iB03p02787>
- Avouac, J.-P., & Tapponnier, P. (1993). Kinematic model of active deformation in central Asia. *Geophysical Research Letters*, 20(10), 895–898. <https://doi.org/https://doi.org/10.1029/93GL00128>
- Bai, M., Chevalier, M.-L., Pan, J., Replumaz, A., Leloup, P. H., Métois, M., & Li, H. (2018). Southeastward increase of the late Quaternary slip-rate of the Xianshuihe fault, eastern Tibet.

- Geodynamic and seismic hazard implications. *Earth and Planetary Science Letters*, 485, 19–31. <https://doi.org/10.1016/j.epsl.2017.12.045>
- Bell, M. A., Elliott, J. R., & Parsons, B. E. (2011). Interseismic strain accumulation across the Manyi fault (Tibet) prior to the 1997 Mw 7.6 earthquake. *Geophysical Research Letters*, 38(24). <https://doi.org/10.1029/2011GL049762>
- Bendick, R., Bilham, R., Khan, M. A., & Khan, S. F. (2007). Slip on an active wedge thrust from geodetic observations of the 8 October 2005 Kashmir earthquake. *Geology*, 35(3), 267–270. Retrieved from <http://geology.gsapubs.org/content/35/3/267.short>
- Berthet, T., Ritz, J.-F., Ferry, M., Pelgat, P., Cattin, R., Drukpa, D., et al. (2014). Active tectonics of the eastern Himalaya: New constraints from the first tectonic geomorphology study in southern Bhutan. *Geology*, 42(5), 427–430. <https://doi.org/10.1130/G35162.1>
- Bian, S., Gong, J., Zuza, A. V., Yang, R., Tian, Y., Ji, J., et al. (2020). Late Pliocene onset of the Cona rift, eastern Himalaya, confirms eastward propagation of extension in Himalayan-Tibetan orogen. *Earth and Planetary Science Letters*, 544, 116383. <https://doi.org/10.1016/j.epsl.2020.116383>
- Bie, L., & Ryder, I. (2014). Recent seismic and aseismic activity in the Ashikule stepover zone, NW Tibet. *Geophysical Journal International*, 198(3), 1632–1643. <https://doi.org/10.1093/gji/ggu230>
- Blisniuk, P. M., & Sharp, W. D. (2003). Rates of late Quaternary normal faulting in central Tibet from U-series dating of pedogenic carbonate in displaced fluvial gravel deposits. *Earth and Planetary Science Letters*, 215(1-2), 169–186. [https://doi.org/10.1016/S0012-821X\(03\)00374-1](https://doi.org/10.1016/S0012-821X(03)00374-1)
- Bollinger, L., Sapkota, S. N., Tapponnier, P., Klinger, Y., Rizza, M., Woerd, J. V. der, et al. (2014). Estimating the return times of great Himalayan earthquakes in eastern Nepal: Evidence from the Patu and Bardibas strands of the Main Frontal Thrust. *Journal of Geophysical Research: Solid Earth*, 119(9), 7123–7163. <https://doi.org/10.1002/2014JB010970>
- Borthakur, A. (2017). An Analysis of the Conflict in the Ferghana Valley. *Asian Affairs*, 48(2), 334–350. <https://doi.org/10.1080/03068374.2017.1313591>
- Brown, E. T. (2005). Comment on "Slip-Rate Measurements on the Karakorum Fault May Imply Secular Variations in Fault Motion". *Science*, 309(5739), 1326b–1326b. <https://doi.org/10.1126/science.1112508>
- Burgess, W. P., Yin, A., Dubey, C. S., Shen, Z.-K., & Kelty, T. K. (2012). Holocene shortening across the Main Frontal Thrust zone in the eastern Himalaya. *Earth and Planetary Science Letters*, 357-358, 152–167. <https://doi.org/10.1016/j.epsl.2012.09.040>
- Burtman, V. S., Skobelev, S. F., & Molnar, P. (1996). Late Cenozoic slip on the Talas-Ferghana fault, the Tien Shan, central Asia. *GSA Bulletin*, 108(8), 1004–1021. [https://doi.org/10.1130/0016-7606\(1996\)108%3C1004:LCSOTT%3E2.3.CO;2](https://doi.org/10.1130/0016-7606(1996)108%3C1004:LCSOTT%3E2.3.CO;2)
- Campbell, G. E., Walker, R. T., Abdurakhmatov, K., Schwenninger, Jl., Jackson, J., Elliott, J. R., & Copley, A. (2013). The Dzhungarian fault: Late Quaternary tectonics and slip rate of a major right-lateral strike-slip fault in the northern Tien Shan region. *Journal of Geophysical Research: Solid Earth*, 118(10), 5681–5698. <https://doi.org/10.1002/jgrb.50367>

- Campbell, G. E., Walker, R. T., Abdurakhmatov, K., Jackson, J., Elliott, J. R., Mackenzie, D., et al. (2015). Great earthquakes in low strain rate continental interiors: An example from SE Kazakhstan. *Journal of Geophysical Research: Solid Earth*, 120(8), 5507–5534. <https://doi.org/10.1002/2015JB011925>
- Charreau, J., Saint-Carlier, D., Dominguez, S., Lavé, J., Blard, P.-H., Avouac, J.-P., et al. (2017). Denudation outpaced by crustal thickening in the eastern Tianshan. *Earth and Planetary Science Letters*, 479, 179–191. <https://doi.org/10.1016/j.epsl.2017.09.025>
- Chase, C. G. (1972). The N Plate Problem of Plate Tectonics. *Geophysical Journal International*, 29(2), 117–122. <https://doi.org/10.1111/j.1365-246X.1972.tb02202.x>
- Chen, G., Xu, X., Wen, X., & Chen, Y.-G. (2016). Late Quaternary Slip-rates and Slip Partitioning on the Southeastern Xianshuihe Fault System, Eastern Tibetan Plateau. *Acta Geologica Sinica - English Edition*, 90(2), 537–554. <https://doi.org/https://doi.org/10.1111/1755-6724.12689>
- Chen, W. (2003). *Principal tectonic deformation features and their generation mechanism in the Hexi Corridor and its adjacent regions since the late Quaternary* ({PhD}). Institute of Geology, China Earthquake Administration, Beijing.
- Chevalier, M.-L., Ryerson, F. J., Tapponnier, P., Finkel, R. C., Woerd, J. V. D., Haibing, L., & Qing, L. (2005). Slip-Rate Measurements on the Karakorum Fault May Imply Secular Variations in Fault Motion. *Science*, 307(5708), 411–414. <https://doi.org/10.1126/science.1105466>
- Chevalier, M.-L., Li, H., Pan, J., Pei, J., Wu, F., Xu, W., et al. (2011). Fast slip-rate along the northern end of the Karakorum fault system, western Tibet. *Geophysical Research Letters*, 38(22). <https://doi.org/10.1029/2011GL049921>
- Chevalier, M.-L., Tapponnier, P., Van der Woerd, J., Ryerson, F. J., Finkel, R. C., & Li, H. (2012). Spatially constant slip rate along the southern segment of the Karakorum fault since 200ka. *Tectonophysics*, 530-531, 152–179. <https://doi.org/10.1016/j.tecto.2011.12.014>
- Chevalier, M.-L., Pan, J., Li, H., Liu, D., & Wang, M. (2015). Quantification of both normal and right-lateral late Quaternary activity along the Kongur Shan extensional system, Chinese Pamir. *Terra Nova*, 27(5), 379–391. <https://doi.org/https://doi.org/10.1111/ter.12170>
- Chevalier, M.-L., Van der Woerd, J., Tapponnier, P., Li, H., Ryerson, F. J., & Finkel, R. C. (2016). Late Quaternary slip-rate along the central Bangong-Chaxikang segment of the Karakorum fault, western Tibet. *GSA Bulletin*, 128(1-2), 284–314. <https://doi.org/10.1130/B31269.1>
- Chevalier, M.-L., Leloup, P. H., Replumaz, A., Pan, J., Liu, D., Li, H., et al. (2016). Tectonic-geomorphology of the Litang fault system, SE Tibetan Plateau, and implication for regional seismic hazard. *Tectonophysics*, 682, 278–292. <https://doi.org/10.1016/j.tecto.2016.05.039>
- Chevalier, M.-L., Pan, J., Li, H., Sun, Z., Liu, D., Pei, J., et al. (2017). First tectonic-geomorphology study along the Longmu–Gozha Co fault system, Western Tibet. *Gondwana Research*, 41, 411–424. <https://doi.org/10.1016/j.gr.2015.03.008>
- Chevalier, M.-L., Leloup, P. H., Replumaz, A., Pan, J., Métois, M., & Li, H. (2018). Temporally constant slip rate along the Ganzi fault, NW Xianshuihe fault system, eastern Tibet. *GSA Bulletin*, 130(3-4), 396–410. <https://doi.org/10.1130/B31691.1>
- Chevalier, M.-L., Tapponnier, P., Woerd, J. van der, Leloup, P. H., Wang, S., Pan, J., et al. (2020). Late Quaternary Extension Rates Across the Northern Half of the Yadong-Gulu Rift: Implication

- for East-West Extension in Southern Tibet. *Journal of Geophysical Research: Solid Earth*, 125(7), e2019JB019106. <https://doi.org/10.1029/2019JB019106>
- Chéry, J., Carretier, S., & Ritz, J.-F. (2001). Postseismic stress transfer explains time clustering of large earthquakes in Mongolia. *Earth and Planetary Science Letters*, 194(1), 277–286.
- Clark, M. K., & Royden, L. H. (2000). Topographic ooze: Building the eastern margin of Tibet by lower crustal flow. *Geology*, 28(8), 703. [https://doi.org/10.1130/0091-7613\(2000\)28%3C703:TOBTEM%3E2.0.CO;2](https://doi.org/10.1130/0091-7613(2000)28%3C703:TOBTEM%3E2.0.CO;2)
- Cowgill, E. (2007). Impact of riser reconstructions on estimation of secular variation in rates of strike-slip faulting: Revisiting the Cherchen River site along the Altyn Tagh Fault, NW China. *Earth and Planetary Science Letters*, 254(3-4), 239–255. <https://doi.org/10.1016/j.epsl.2006.09.015>
- Cowgill, E., Yin, A., Feng, W. X., & Qing, Z. (2000). Is the North Altyn fault part of a strike-slip duplex along the Altyn Tagh fault system? *Geology*, 28(3), 255–258.
- Cox, A., & Hart, R. B. (1986). *Plate tectonics: How it works*. Palo Alto: Blackwell Scientific Publications.
- Cunningham, D. (2013). Mountain building processes in intracontinental oblique deformation belts: Lessons from the Gobi Corridor, Central Asia. *Journal of Structural Geology*, 46, 255–282. <https://doi.org/10.1016/j.jsg.2012.08.010>
- Davis, T. A. (2004). Algorithm 832: UMFPACK V4.3—an unsymmetric-pattern multifrontal method. *ACM Transactions on Mathematical Software*, 30(2), 196–199. <https://doi.org/10.1145/992200.992206>
- Densmore, A. L., Ellis, M. A., Li, Y., Zhou, R., Hancock, G. S., & Richardson, N. (2007). Active tectonics of the Beichuan and Pengguan faults at the eastern margin of the Tibetan Plateau. *Tectonics*, 26(4). [https://doi.org/https://doi.org/10.1029/2006TC001987](https://doi.org/10.1029/2006TC001987)
- Ding, L., Zhong, D., Yin, A., Kapp, P., & Harrison, T. M. (2001). Cenozoic structural and metamorphic evolution of the eastern Himalayan syntaxis (Namche Barwa). *Earth and Planetary Science Letters*, 192(3), 423–438. [https://doi.org/10.1016/S0012-821X\(01\)00463-0](https://doi.org/10.1016/S0012-821X(01)00463-0)
- Dolan, J. F., & Meade, B. J. (2017). A Comparison of Geodetic and Geologic Rates Prior to Large Strike-Slip Earthquakes: A Diversity of Earthquake-Cycle Behaviors? *Geochemistry, Geophysics, Geosystems*, 18(12), 4426–4436. <https://doi.org/10.1002/2017GC007014>
- Duvall, A. R., & Clark, M. K. (2010). Dissipation of fast strike-slip faulting within and beyond northeastern Tibet. *Geology*, 38(3), 223–226.
- Elliott, A. J., Osokin, M. E., Liu-zeng, J., & Shao, Y.-X. (2018). Persistent rupture terminations at a restraining bend from slip rates on the eastern Altyn Tagh fault. *Tectonophysics*, 733, 57–72. <https://doi.org/10.1016/j.tecto.2018.01.004>
- Funning, G. J., Parsons, B., & Wright, T. J. (2007). Fault slip in the 1997 Manyi, Tibet earthquake from linear elastic modelling of InSAR displacements. *Geophysical Journal International*, 169(3), 988–1008. <https://doi.org/10.1111/j.1365-246X.2006.03318.x>
- Gan, W., Zhang, P., Shen, Z.-K., Niu, Z., Wang, M., Wan, Y., et al. (2007). Present-day crustal motion within the Tibetan Plateau inferred from GPS measurements. *Journal of Geophysical Research*, 112(B8). <https://doi.org/10.1029/2005JB004120>

- Garthwaite, M. C., Wang, H., & Wright, T. J. (2013). Broadscale interseismic deformation and fault slip rates in the central Tibetan Plateau observed using InSAR. *Journal of Geophysical Research: Solid Earth*, 118(9), 5071–5083. <https://doi.org/10.1002/jgrb.50348>
- Gold, R. D., Cowgill, E., Arrowsmith, J. R., Gosse, J., Chen, X., & Wang, X. (2009). Riser diachroneity, lateral erosion, and uncertainty in rates of strike-slip faulting: A case study from Tuzidun along the Altyn Tagh Fault, NW China. *Journal of Geophysical Research*, 114(B4). <https://doi.org/10.1029/2008JB005913>
- Gulliksson, M., & Wedin, P. (1992). Modifying the QR-Decomposition to Constrained and Weighted Linear Least Squares. *SIAM Journal on Matrix Analysis and Applications*, 13(4), 1298–1313. <https://doi.org/10.1137/0613079>
- Ha, G., Wu, Z., & Liu, F. (2019). Late Quaternary vertical slip rates along the Southern Yadong–Gulu Rift, Southern Tibetan Plateau. *Tectonophysics*, 755, 75–90. <https://doi.org/10.1016/j.tecto.2019.02.014>
- Harkins, N., Kirby, E., Shi, X., Wang, E., Burbank, D., & Chun, F. (2010). Millennial slip rates along the eastern Kunlun fault: Implications for the dynamics of intracontinental deformation in Asia. *Lithosphere*, 2(4), 247–266. <https://doi.org/10.1130/L85.1>
- He, H.-L., & Ikeda, Y. (2007). Faulting on the Anninghe fault zone, Southwest China in Late Quaternary and its movement model. *Acta Seismologica Sinica*, 20(5), 571–583. <https://doi.org/10.1007/s11589-007-0571-4>
- He, H.-L., Ikeda, Y., He, Y., Togo, M., Chen, J., Chen, C., et al. (2008). Newly-generated Daliangshan fault zone — Shortcutting on the central section of Xianshuihe-Xiaojiang fault system. *Science in China Series D: Earth Sciences*, 51(9), 1248–1258. <https://doi.org/10.1007/s11430-008-0094-4>
- Hetland, E. A., & Hager, B. H. (2005). Postseismic and interseismic displacements near a strike-slip fault: A two-dimensional theory for general linear viscoelastic rheologies. *Journal of Geophysical Research*, 110(B10). <https://doi.org/10.1029/2005JB003689>
- Hilley, G. E., Johnson, K. M., Wang, M., Shen, Z.-K., & Bürgmann, R. (2009). Earthquake-cycle deformation and fault slip rates in northern Tibet. *Geology*, 37(1), 31–34. <https://doi.org/10.1130/G25157A.1>
- Hollingsworth, J., Wernicke, B. P., & Ding, L. (2010). Fault slip-rate estimate for the right-lateral Beng Co strike-slip fault, based on Quaternary dating of displaced paleo-lake shorelines. *AGU Fall Meeting Abstracts*, 43, T43C–2229. Retrieved from <http://adsabs.harvard.edu/abs/2010AGUFM.T43C2229H>
- Huang, X., Jing, Z., Xie, F., & Zhao, J. (2019). Late quaternary slip rate of the east segment of the Yushu fault in the central-eastern Tibetan Plateau. *Quaternary International*, 532, 146–156. <https://doi.org/10.1016/j.quaint.2019.11.029>
- Jarrard, R. D. (1986). Relations among subduction parameters. *Reviews of Geophysics*, 24(2), 217. <https://doi.org/10.1029/RG024i002p00217>
- Jiang, W., Han, Z., Guo, P., Zhang, J., Jiao, Q., Kang, S., & Tian, Y. (2017). Slip rate and recurrence intervals of the east Lenglongling fault constrained by morphotectonics: Tectonic implications for the northeastern Tibetan Plateau. *Lithosphere*, 9(3), 417–430. <https://doi.org/10.1130/L597.1>

- Jouanne, F., Mugnier, J. L., Gamond, J. F., Fort, P. L., Pandey, M. R., Bollinger, L., et al. (2004). Current shortening across the Himalayas of Nepal. *Geophysical Journal International*, 157(1), 1–14. <https://doi.org/10.1111/j.1365-246X.2004.02180.x>
- Kirby, E., Whipple, K. X., Burchfiel, B. C., Tang, W., Berger, G., Sun, Z., & Chen, Z. (2000). Neotectonics of the Min Shan, China: Implications for mechanisms driving Quaternary deformation along the eastern margin of the Tibetan Plateau. *Geological Society of America Bulletin*, 112(3), 375–393. [https://doi.org/10.1130/0016-7606\(2000\)112%3C375:NOTMSC%3E2.0.CO;2](https://doi.org/10.1130/0016-7606(2000)112%3C375:NOTMSC%3E2.0.CO;2)
- Kirby, Eric, Harkins, N., Wang, E., Shi, X., Fan, C., & Burbank, D. (2007). Slip rate gradients along the eastern Kunlun fault. *Tectonics*, 26(2). <https://doi.org/https://doi.org/10.1029/2006TC002033>
- Klinger, Y., Etchebe, M., Tapponnier, P., & Narteau, C. (2011). Characteristic slip for five great earthquakes along the Fuyun fault in China. *Nature Geoscience*, 4(6), 389–392. <https://doi.org/10.1038/ngeo1158>
- Kong, P., Fink, D., Na, C., & Xiao, W. (2010). Dip-slip rate determined by cosmogenic surface dating on a Holocene scarp of the Daju fault, Yunnan, China. *Tectonophysics*, 493(1), 106–112. <https://doi.org/10.1016/j.tecto.2010.07.006>
- Kreemer, C., Blewitt, G., & Klein, E. C. (2014). A geodetic plate motion and Global Strain Rate Model. *Geochemistry, Geophysics, Geosystems*, 15(10), 3849–3889. <https://doi.org/10.1002/2014GC005407>
- Kumar, S., Wesnousky, S. G., Rockwell, T. K., Ragona, D., Thakur, V. C., & Seitz, G. G. (2001). Earthquake Recurrence and Rupture Dynamics of Himalayan Frontal Thrust, India. *Science*, 294(5550), 2328–2331. <https://doi.org/10.1126/science.1066195>
- Kundu, B., Yadav, R. K., Bali, B. S., Chowdhury, S., & Gahalaut, V. K. (2014). Oblique convergence and slip partitioning in the NW Himalaya: Implications from GPS measurements: NW HIMALAYAN TECTONICS. *Tectonics*, 33(10), 2013–2024. <https://doi.org/10.1002/2014TC003633>
- Lavé, J., & Avouac, J. P. (2000). Active folding of fluvial terraces across the Siwaliks Hills, Himalayas of central Nepal. *Journal of Geophysical Research: Solid Earth*, 105(B3), 5735–5770. <https://doi.org/10.1029/1999JB900292>
- Lensen, G. J. (1964). The General Case of Progressive Fault Displacement of Flights of Degradational Terraces. *New Zealand Journal of Geology and Geophysics*, 7(4), 864–870. <https://doi.org/10.1080/00288306.1964.10428134>
- Li, C., Zhang, P., Yin, J., & Min, W. (2009). Late Quaternary left-lateral slip rate of the Haiyuan fault, northeastern margin of the Tibetan Plateau. *Tectonics*, 28(5). <https://doi.org/10.1029/2008TC002302>
- Li, H., Zhang, Y., Dong, S., Zhang, J., Sun, Y., & Wang, Q. (2020). Neotectonics of the Bailongjiang and Hanan faults: New insights into late Cenozoic deformation along the eastern margin of the Tibetan Plateau. *GSA Bulletin*, 132(9-10), 1845–1862. <https://doi.org/10.1130/B35374.1>
- Li, K., Wang, D., Shao, Q.-F., & Xu, X. (2018). Holocene slip rate along the NE-trending Qixiang Co fault in the central Tibetan Plateau and its tectonic implications. *Seismology and Geology*, 40(6), 1204–1215. <https://doi.org/10.3969/j.issn.0253-4967.2018.06.002>

- Li, K., Kirby, E., Xu, X., Chen, G., Ren, J., & Wang, D. (2019). Rates of Holocene normal faulting along the Dong Co fault in central Tibet, based on ^{14}C dating of displaced fluvial terraces. *Journal of Asian Earth Sciences*, 183, 103962. <https://doi.org/10.1016/j.jseaes.2019.103962>
- Li, X., Li, C., Wesnousky, S. G., Zhang, P., Zheng, W., Pierce, I. K. D., & Wang, X. (2017). Paleoseismology and slip rate of the western Tianjingshan fault of NE Tibet, China. *Journal of Asian Earth Sciences*, 146, 304–316. <https://doi.org/10.1016/j.jseaes.2017.04.031>
- Li, Z., Elliott, J. R., Feng, W., Jackson, J. A., Parsons, B. E., & Walters, R. J. (2011). The 2010 MW 6.8 Yushu (Qinghai, China) earthquake: Constraints provided by InSAR and body wave seismology. *Journal of Geophysical Research: Solid Earth*, 116(B10). <https://doi.org/https://doi.org/10.1029/2011JB008358>
- Lin, A., & Guo, J. (2008). Nonuniform Slip Rate and Millennial Recurrence Interval of Large Earthquakes along the Eastern Segment of the Kunlun Fault, Northern Tibet. *Bulletin of the Seismological Society of America*, 98(6), 2866–2878. <https://doi.org/10.1785/0120070193>
- Liu, D., Li, H., Sun, Z., Pan, J., Wang, M., Wang, H., & Marie-LuceChevalier. (2017). AFT dating constrains the Cenozoic uplift of the Qimen Tagh Mountains, Northeast Tibetan Plateau, comparison with LA-ICPMS Zircon U-Pb ages. *Gondwana Research*, 41, 438–450. <https://doi.org/10.1016/j.gr.2015.10.008>
- Liu-Zeng, J., Klinger, Y., Xu, X., Lasserre, C., Chen, G., Chen, W., et al. (2007). Millennial Recurrence of Large Earthquakes on the Haiyuan Fault near Songshan, Gansu Province, China. *Bulletin of the Seismological Society of America*, 97(1B), 14–34. <https://doi.org/10.1785/0120050118>
- Malik, J. N., & Nakata, T. (2003). Active faults and related Late Quaternary deformation along the Northwestern Himalayan Frontal Zone, India. Retrieved from <https://www.earthprints.org/handle/2122/996>
- Malik, Javed N., Sahoo, S., Satuluri, S., & Okumura, K. (2015). Active Fault and Paleoseismic Studies in Kangra Valley: Evidence of Surface Rupture of a Great Himalayan 1905 Kangra Earthquake (Mw 7.8), Northwest Himalaya, India. *Bulletin of the Seismological Society of America*, 105(5), 2325–2342. <https://doi.org/10.1785/0120140304>
- McCaffrey, R. (1994). Global variability in subduction thrust zone-forearc systems. *Pure and Applied Geophysics*, 142(1), 173–224. <https://doi.org/10.1007/BF00875971>
- McCaffrey, R., & Nabelek, J. (1998). Role of oblique convergence in the active deformation of the Himalayas and southern Tibet plateau. *Geology*, 26(8), 691–694. Retrieved from <http://geology.gsapubs.org/content/26/8/691.short>
- Meade, B. J., & Loveless, J. P. (2009). Block Modeling with Connected Fault-Network Geometries and a Linear Elastic Coupling Estimator in Spherical Coordinates. *Bulletin of the Seismological Society of America*, 99(6), 3124–3139. <https://doi.org/10.1785/0120090088>
- Metzger, S., Ischuk, A., Deng, Z., Ratschbacher, L., Perry, M., Kufner, S.-K., et al. (2020). Dense GNSS Profiles Across the Northwestern Tip of the India-Asia Collision Zone: Triggered Slip and Westward Flow of the Peter the First Range, Pamir, Into the Tajik Depression. *Tectonics*, 39(2), e2019TC005797. <https://doi.org/10.1029/2019TC005797>
- Meyer, B., Tapponnier, P., Bourjot, L., Métivier, F., Gaudemer, Y., Peltzer, G., et al. (1998). Crustal thickening in Gansu-Qinghai, lithospheric mantle subduction, and oblique, strike-slip

- controlled growth of the Tibet plateau. *Geophysical Journal International*, 135(1), 1–47. <https://doi.org/10.1046/j.1365-246X.1998.00567.x>
- Min, S., Watkinson, I. M., Tun, S. T., Naing, W., & Swe, T. L. (2017). The Kyaukkyan Fault, Myanmar. *Geological Society, London, Memoirs*, 48(1), 453–471. <https://doi.org/10.1144/M48.21>
- Min, W., Zhang, P., He, W., Li, C., Mao, F., & Zhang, S. (2002). Research on the active faults and paleoearthquakes in the western Jiuquan basin. *Seismology and Geology*, 24(1), 35–44.
- Mohadjer, S., Bendick, R., Ischuk, A., Kuzikov, S., Kostuk, A., Saydullaev, U., et al. (2010). Partitioning of India-Eurasia convergence in the Pamir-Hindu Kush from GPS measurements. *Geophysical Research Letters*, 37(4), L04305. <https://doi.org/10.1029/2009GL041737>
- Murphy, M. A., Taylor, M. H., Gosse, J., Silver, C. R. P., Whipp, D. M., & Beaumont, C. (2014). Limit of strain partitioning in the Himalaya marked by large earthquakes in western Nepal. *Nature Geoscience*, 7(1), 38–42. <https://doi.org/10.1038/ngeo2017>
- Nakata, T. (1989). Active faults of the Himalaya of India and Nepal. In *Geological Society of America Special Papers* (Vol. 232, pp. 243–264). Geological Society of America. <https://doi.org/10.1130/SPE232-p243>
- Peltzer, G., & Tapponnier, P. (1988). Formation and evolution of strike-slip faults, rifts, and basins during the India-Asia Collision: An experimental approach. *Journal of Geophysical Research: Solid Earth*, 93(B12), 15085–15117. <https://doi.org/10.1029/JB093iB12p15085>
- Powers, P. M., Lillie, R. J., & Yeats, R. S. (1998). Structure and shortening of the Kangra and Dehra Dun reentrants, Sub-Himalaya, India. *GSA Bulletin*, 110(8), 1010–1027. [https://doi.org/10.1130/0016-7606\(1998\)110%3C1010:SASOTK%3E2.3.CO;2](https://doi.org/10.1130/0016-7606(1998)110%3C1010:SASOTK%3E2.3.CO;2)
- Priyanka, R. S., Jayangondaperumal, R., Pandey, A., Mishra, R. L., Singh, I., Bhushan, R., et al. (2017). Primary surface rupture of the 1950 Tibet-Assam great earthquake along the eastern Himalayan front, India. *Scientific Reports*, 7(1), 5433. <https://doi.org/10.1038/s41598-017-05644-y>
- Rao, G., Lin, A., Yan, B., Jia, D., & Wu, X. (2014). Tectonic activity and structural features of active intracontinental normal faults in the Weihe Graben, central China. *Tectonophysics*, 636, 270–285. <https://doi.org/10.1016/j.tecto.2014.08.019>
- Ren, J., Xu, X., Yeats, R. S., & Zhang, S. (2013a). Latest Quaternary paleoseismology and slip rates of the Longriba fault zone, eastern Tibet: Implications for fault behavior and strain partitioning. *Tectonics*, 32(2), 216–238. [https://doi.org/https://doi.org/10.1002/tect.20029](https://doi.org/10.1029/tect.20029)
- Ren, J., Xu, X., Yeats, R. S., & Zhang, S. (2013b). Millennial slip rates of the Tazang fault, the eastern termination of Kunlun fault: Implications for strain partitioning in eastern Tibet. *Tectonophysics*, 608, 1180–1200. <https://doi.org/10.1016/j.tecto.2013.06.026>
- Rizza, M., Abdurakhmatov, K., Walker, R., Braucher, R., Guillou, V., Carr, A. S., et al. (2019). Rate of Slip From Multiple Quaternary Dating Methods and Paleoseismic Investigations Along the Talas-Fergana Fault: Tectonic Implications for the Tien Shan Range. *Tectonics*, 38(7), 2477–2505. <https://doi.org/10.1029/2018TC005188>
- Robinson, A. C. (2009). Evidence against Quaternary slip on the northern Karakorum Fault suggests kinematic reorganization at the western end of the Himalayan-Tibetan orogen. *Earth*

and Planetary Science Letters, 286(1-2), 158–170. <https://doi.org/10.1016/j.epsl.2009.06.025>

- Rust, D., Korzhenkov, A., & Tibaldi, A. (2018). Geologic Slip-Rate Determinations on the Talas-Fergana Fault: Mismatch With Geodetic Slip Rate. *Geophysical Research Letters*, 45(9), 3880–3888. <https://doi.org/10.1002/2017GL076990>
- Sanchez, V. I., Murphy, M. A., Robinson, A. C., Lapen, T. J., & Heizler, M. T. (2013). Tectonic evolution of the India–Asia suture zone since Middle Eocene time, Lopukangri area, south-central Tibet. *Journal of Asian Earth Sciences*, 62, 205–220. <https://doi.org/10.1016/j.jseaes.2012.09.004>
- Scharer, K. M., Burbank, D. W., Chen, J., Weldon, R. J., Rubin, C., Zhao, R., & Shen, J. (2004). Detachment folding in the Southwestern Tian Shan–Tarim foreland, China: Shortening estimates and rates. *Journal of Structural Geology*, 26(11), 2119–2137. <https://doi.org/10.1016/j.jsg.2004.02.016>
- Schlupp, A., & Cisternas, A. (2007). Source history of the 1905 great Mongolian earthquakes (Tsetserleg, Bolnay). *Geophysical Journal International*, 169(3), 1115–1131. <https://doi.org/10.1111/j.1365-246X.2007.03323.x>
- Schoenbohm, L. M., Burchfiel, B. C., Liangzhong, C., & Jiyun, Y. (2006). Miocene to present activity along the Red River fault, China, in the context of continental extrusion, upper-crustal rotation, and lower-crustal flow. *GSA Bulletin*, 118(5-6), 672–688. <https://doi.org/10.1130/B25816.1>
- Shah, A. A., Rajasekharan, A., Batmanathan, N., Farhan, Z., & Malik, J. N. (2021). Dras Fault: A major active fault in Kashmir Himalaya, 9.
- Shi, X., Kirby, E., Lu, H., Robinson, R., Furlong, K. P., & Wang, E. (2014). Holocene slip rate along the Gyaring Co Fault, central Tibet. *Geophysical Research Letters*, 41(16), 5829–5837. <https://doi.org/10.1002/2014GL060782>
- Silver, C. R. P., Murphy, M. A., Taylor, M. H., Gosse, J., & Baltz, T. (2015). Neotectonics of the Western Nepal Fault System: Implications for Himalayan strain partitioning. *Tectonics*, 34(12), 2494–2513. <https://doi.org/10.1002/2014TC003730>
- Soto, G. L., Sandvol, E., Ni, J. F., Flesch, L., Hearn, T. M., Tilmann, F., et al. (2012). Significant and vertically coherent seismic anisotropy beneath eastern Tibet. *Journal of Geophysical Research: Solid Earth*, 117(B5). [https://doi.org/https://doi.org/10.1029/2011JB008919](https://doi.org/10.1029/2011JB008919)
- Stevens, V. L., & Avouac, J. P. (2015). Interseismic coupling on the main Himalayan thrust. *Geophysical Research Letters*, 42(14), 5828–5837. <https://doi.org/10.1002/2015GL064845>
- Styron, R. (2019). The impact of earthquake cycle variability on neotectonic and paleoseismic slip rate estimates. *Solid Earth*, 10(1), 15–25. <https://doi.org/https://doi.org/10.5194/se-10-15-2019>
- Styron, R., & Pagani, M. (2020). The GEM Global Active Faults Database. *Earthquake Spectra*, 8755293020944182. <https://doi.org/10.1177/8755293020944182>
- Styron, R., Taylor, M., & Okoronkwo, K. (2010). Database of Active Structures From the Indo-Asian Collision. *Eos, Transactions American Geophysical Union*, 91(20), 181–182. <https://doi.org/10.1029/2010EO200001>

- Styron, R., Poggi, V., & Lunina, O. V. (2018). GEM Northeastern Asia Active Fault Database. Global Earthquake Model Foundation. <https://doi.org/10.13117/NE-ASIA-ACTIVE-FAULTS>
- Styron, R., García-Pelaez, J., & Pagani, M. (2020). CCAF-DB: The Caribbean and Central American active fault database. *Natural Hazards and Earth System Sciences*, 20(3), 831–857. <https://doi.org/https://doi.org/10.5194/nhess-20-831-2020>
- Styron, R. H., Taylor, M. H., & Murphy, M. A. (2011). Oblique convergence, arc-parallel extension, and the role of strike-slip faulting in the High Himalaya. *Geosphere*, 7(2), 582–596. Retrieved from <http://geosphere.gsapubs.org/content/7/2/582.short>
- Styron, R. H., Taylor, M. H., Sundell, K. E., Stockli, D. F., Oalmann, J. A. G., Möller, A., et al. (2013). Miocene initiation and acceleration of extension in the South Lunggar rift, western Tibet: Evolution of an active detachment system from structural mapping and (U-Th)/He thermochronology: SOUTH LUNGGAR RIFT, SW TIBET. *Tectonics*, n/a-n/a. <https://doi.org/10.1002/tect.20053>
- Sundell, K. E., Taylor, M. H., Styron, R. H., Stockli, D. F., Kapp, P., Hager, C., et al. (2013). Evidence for constriction and Pliocene acceleration of east-west extension in the North Lunggar rift region of west central Tibet: NORTH LUNGGAR RIFT, WEST CENTRAL TIBET. *Tectonics*, 32(5), 1454–1479. <https://doi.org/10.1002/tect.20086>
- Tapponnier, P., & Molnar, P. (1979). Active faulting and Cenozoic tectonics of the Tien Shan, Mongolia, and Baykal Regions. *Journal of Geophysical Research: Solid Earth*, 84(B7), 3425–3459. <https://doi.org/10.1029/JB084iB07p03425>
- Taylor, M., & Peltzer, G. (2006). Current slip rates on conjugate strike-slip faults in central Tibet using synthetic aperture radar interferometry: STRIKE-SLIP SAR RATES, CENTRAL TIBET. *Journal of Geophysical Research: Solid Earth*, 111(B12), n/a-n/a. <https://doi.org/10.1029/2005JB004014>
- Taylor, M., & Yin, A. (2009). Active structures of the Himalayan-Tibetan orogen and their relationships to earthquake distribution, contemporary strain field, and Cenozoic volcanism. *Geosphere*, 5(3), 199–214.
- Taylor, M., Yin, A., Ryerson, F. J., Kapp, P., & Ding, L. (2003). Conjugate strike-slip faulting along the Bangong-Nujiang suture zone accommodates coeval east-west extension and north-south shortening in the interior of the Tibetan Plateau: CONJUGATE STRIKE-SLIP FAULTING WITHIN TIBET. *Tectonics*, 22(4), n/a-n/a. <https://doi.org/10.1029/2002TC001361>
- Thompson Jobe, J. A., Li, T., Chen, J., Burbank, D. W., & Bufo, A. (2017). Quaternary tectonic evolution of the Pamir-Tian Shan convergence zone, Northwest China. *Tectonics*, 36(12), 2748–2776. <https://doi.org/10.1002/2017TC004541>
- Thompson, S. C., Weldon, R. J., Rubin, C. M., Abdurakhmatov, K., Molnar, P., & Berger, G. W. (2002). Late Quaternary slip rates across the central Tien Shan, Kyrgyzstan, central Asia. *Journal of Geophysical Research: Solid Earth*, 107(B9), ETG 7-1-ETG 7-32. <https://doi.org/10.1029/2001JB000596>
- Van der Woerd, J., Ryerson, F. J., Tapponnier, P., Gaudemer, Y., Finkel, R., Meriaux, A. S., et al. (1998). Holocene left-slip rate determined by cosmogenic surface dating on the Xidatan segment of the Kunlun fault (Qinghai, China). *Geology*, 26(8), 695–698. [https://doi.org/10.1130/0091-7613\(1998\)026%3C0695:HLSRDB%3E2.3.CO;2](https://doi.org/10.1130/0091-7613(1998)026%3C0695:HLSRDB%3E2.3.CO;2)

- Van der Woerd, J., Xu, X., Li, H., Tapponnier, P., Meyer, B., Ryerson, F. J., et al. (2001). Rapid active thrusting along the northwestern range front of the Tanghe Nan Shan (western Gansu, China). *Journal of Geophysical Research: Solid Earth*, 106(B12), 30475–30504. <https://doi.org/10.1029/2001JB000583>
- Van der Woerd, J. V. der, Ryerson, F. J., Tapponnier, P., Meriaux, A.-S., Gaudemer, Y., Meyer, B., et al. (2000). Uniform slip-rate along the Kunlun Fault: Implications for seismic behaviour and large-scale tectonics. *Geophysical Research Letters*, 27(16), 2353–2356. <https://doi.org/10.1029/1999GL011292>
- Vigny, C., Socquet, A., Rangin, C., Chamot-Rooke, N., Pubellier, M., Bouin, M.-N., et al. (2003). Present-day crustal deformation around Sagaing fault, Myanmar. *Journal of Geophysical Research: Solid Earth*, 108(B11). <https://doi.org/10.1029/2002JB001999>
- Volkmer, J. E., Kapp, P., Guynn, J. H., & Lai, Q. (2007). Cretaceous-Tertiary structural evolution of the north central Lhasa terrane, Tibet. *Tectonics*, 26(6), n/a–n/a. <https://doi.org/10.1029/2005TC001832>
- Wang, E., & Burchfiel, B. C. (2000). Late Cenozoic to Holocene deformation in southwestern Sichuan and adjacent Yunnan, China, and its role in formation of the southeastern part of the Tibetan Plateau. *GSA Bulletin*, 112(3), 413–423. [https://doi.org/10.1130/0016-7606\(2000\)112%3C413:LCTHDI%3E2.0.CO;2](https://doi.org/10.1130/0016-7606(2000)112%3C413:LCTHDI%3E2.0.CO;2)
- Wang, G., Wan, J., Wang, E., Zheng, D., & Li, F. (2008). Late Cenozoic to recent transtensional deformation across the Southern part of the Gaoligong shear zone between the Indian plate and SE margin of the Tibetan plateau and its tectonic origin. *Tectonophysics*, 460(1), 1–20. <https://doi.org/10.1016/j.tecto.2008.04.007>
- Wang, H., Wright, T. J., Liu-Zeng, J., & Peng, L. (2019). Strain Rate Distribution in South-Central Tibet From Two Decades of InSAR and GPS. *Geophysical Research Letters*, 46(10), 5170–5179. <https://doi.org/10.1029/2019GL081916>
- Wang, K., Zhu, Y., Nissen, E., & Shen, Z.-K. (2021). On the Relevance of Geodetic Deformation Rates to Earthquake Potential. *Geophysical Research Letters*, 48(11), e2021GL093231. <https://doi.org/10.1029/2021GL093231>
- Wang, M., & Shen, Z.-K. (2020). Present-Day Crustal Deformation of Continental China Derived From GPS and Its Tectonic Implications. *Journal of Geophysical Research: Solid Earth*, 125(2), e2019JB018774. <https://doi.org/10.1029/2019JB018774>
- Wang, S., Chevalier, M.-L., Pan, J., Bai, M., Li, K., Li, H., & Wang, G. (2020). Quantification of the late Quaternary throw rates along the Yadong rift, southern Tibet. *Tectonophysics*, 790, 228545. <https://doi.org/10.1016/j.tecto.2020.228545>
- Wang, Y., Wang, P., Ge, W., Zhou, R., Schoenbohm, L. M., Zhang, B., et al. (2019). Differential crustal deformation across the Cona-Oiga rift, southern Tibetan Plateau. *Journal of Asian Earth Sciences*, 177, 177–185. <https://doi.org/10.1016/j.jseas.2019.03.023>
- Wesnousky, S. G., Kumar, S., Mohindra, R., & Thakur, V. C. (1999). Uplift and convergence along the Himalayan Frontal Thrust of India. *Tectonics*, 18(6), 967–976. <https://doi.org/10.1029/1999TC900026>
- Xu, Xiwei, Wen, X., Zheng, R., Ma, W., Song, F., & Yu, G. (2003). Pattern of latest tectonic motion and its dynamics for active blocks in Sichuan-Yunnan region, China. *Science in China Series D*:

Earth Sciences, 46(2), 210–226. <https://doi.org/10.1360/03dz0017>

- Xu, Xiwei, Wen, X., Yu, G., Zheng, R., Luo, H., & Zheng, B. (2005). Average slip rate, earthquake rupturing segmentation and recurrence behavior on the Litang fault zone, western Sichuan Province, China. *Science in China Series D: Earth Sciences*, 48(8), 1183–1196. <https://doi.org/10.1360/04yd0072>
- Xu, XiWei, Wen, X., Chen, G., & Yu, G. (2008). Discovery of the Longriba Fault Zone in Eastern Bayan Har Block, China and its tectonic implication. *Science in China Series D-Earth Sciences*, 51(9), 1209–1223. <https://doi.org/10.1007/s11430-008-0097-1>
- Xu, Xiwei, Wen, X., Yu, G., Chen, G., Klinger, Y., Hubbard, J., & Shaw, J. (2009). Coseismic reverse-and oblique-slip surface faulting generated by the 2008 Mw 7.9 Wenchuan earthquake, China. *Geology*, 37(6), 515–518. Retrieved from <http://geology.gsapubs.org/content/37/6/515.short>
- Yin, A., Dang, Y.-Q., Wang, L.-C., Jiang, W.-M., Zhou, S.-P., Chen, X.-H., et al. (2008). Cenozoic tectonic evolution of Qaidam basin and its surrounding regions (Part 1): The southern Qilian Shan-Nan Shan thrust belt and northern Qaidam basin. *Geological Society of America Bulletin*, 120(7-8), 813–846. Retrieved from <http://gsabulletin.gsapubs.org/content/120/7-8/813.short>
- Yuan, D.-Y., Champagnac, J.-D., Ge, W.-P., Molnar, P., Zhang, P.-Z., Zheng, W.-J., et al. (2011). Late Quaternary right-lateral slip rates of faults adjacent to the lake Qinghai, northeastern margin of the Tibetan Plateau. *GSA Bulletin*, 123(9-10), 2016–2030. <https://doi.org/10.1130/B30315.1>
- Yuan, Z., Liu-Zeng, J., Wang, W., Weldon, R. J., Oskin, M. E., Shao, Y., et al. (2018). A 6000-year-long paleoseismologic record of earthquakes along the Xorkoli section of the Altyn Tagh fault, China. *Earth and Planetary Science Letters*, 497, 193–203. <https://doi.org/10.1016/j.epsl.2018.06.008>
- Zhang, G., Qu, C., Shan, X., Song, X., Zhang, G., Wang, C., et al. (2011). Slip distribution of the 2008 Wenchuan Ms 7.9 earthquake by joint inversion from GPS and InSAR measurements: A resolution test study: Slip distribution of 2008 Wenchuan earthquake. *Geophysical Journal International*, 186(1), 207–220. <https://doi.org/10.1111/j.1365-246X.2011.05039.x>
- Zheng, W., Zhang, P., He, W., Yuan, D., Shao, Y., Zheng, D., et al. (2013). Transformation of displacement between strike-slip and crustal shortening in the northern margin of the Tibetan Plateau: Evidence from decadal GPS measurements and late Quaternary slip rates on faults. *Tectonophysics*, 584, 267–280. <https://doi.org/10.1016/j.tecto.2012.01.006>
- Zubovich, A. V., Wang, X., Scherba, Y. G., Schelochkov, G. G., Reilinger, R., Reigber, C., et al. (2010). GPS velocity field for the Tien Shan and surrounding regions. *Tectonics*, 29(6). <https://doi.org/https://doi.org/10.1029/2010TC002772>